UNIVERSITÀ DEGLI STUDI DI NAPOLI
FEDERICO II

International PhD program on

Novel technologies for Materials, Sensors and Imaging

XXIV cycle

SQUID based multichannel system for brain functional imaging

by

Antonio Vettoliere

Coordinator: prof. Antonello Andreone

November 2012

Antonio Vettoliere

SQUID based multichannel system for brain imaging

A thesis submitted at Università degli Studi di Napoli "Federico II" in fulfillment of the requirements for the degree of PHILOSOPHIAE DOCTOR in Novel Technologies for Materials, Sensors, and Imaging.

The experimental activities described in this thesis have been carried out at Istituto di Cibernetica "E. Caianiello" of Consiglio Nazionale delle Ricerche, (ICIB-CNR) Pozzuoli (Napoli - Italy).

Coordinator: prof. Antonello Andreone

Tutors: Dr. Carmine Granata (ICIB-CNR)
            Dr. Maurizio Russo (ICIB-CNR)

To my family

Table of contents

Introduction

The human brain is a very complex structure and represents the main part of the central nervous system. It contain at least 20 billions different types of neurons half of which in the cerebral cortex.

Each neuron has a proper function related to its intrinsic properties and to aptitude to manage the signals coming from other neuronal group.

In the information processing, small currents flow in the neural system and produce a weak magnetic field which can be measured, in a completely non invasive way, by a suitable sensor, placed outside the skull. This method of brain magnetic field recording, called magneto-encephalography (MEG) provides useful information about its functionality, identifying the brain area that is activated by an external stimulus or due to a spontaneous brain activity.

The intensity of magnetic field related to the brain activity is very low, being, close to the scalp, few tens fT for the evoked activity and about 1 fT in the case of the spontaneous one. So, all background magnetic fields are higher than the signals to measure. These considerations lead to two requirements: Extremely high sensitive sensors and systems to reject the background noise are needed.

Nowadays, the best sensor to detect the weak magnetic field produced by the human brain is a Superconducting QUantum Interference Device (SQUID) which is able to detect a magnetic field as low as few *fT* per bandwidth unit. In addition, to avoid any background noise, both high permeability shielding room and sophisticated noise cancellation techniques must be employed. Nevertheless, in order to obtain an acceptable signal/noise ratio either hardware or electronic gradiometers are typically used.

The first SQUID measurement of magnetic fields of the brain was carried out by David Cohen (1972). He measured the spontaneous activity of a healthy subject comparing it to the abnormal brain activity of an epileptic patient. Evoked responses were first recorded a few years later (1975).

SQUID magnetometers are used also to detect magnetic fields arising from heart activity (Magnetocardiography – MCG) and to measure the paramagnetic substance concentration in specific organs (liver, heart) by applying a

magnetic field (Biosusceptometry) or more generally in the whole area of research referred as biomagnetism.

In the first section of this thesis, the basics of magnetoencephalography will be briefly addressed taking into account the mathematical models used to schematize neuronal signals (dipole models) and to rebuild the electric currents starting from the measured magnetic field outside the head. Furthermore, the architecture of the biomagnetic systems will be discussed and the main application of magnetoencephalography will be described in view of both clinical applications and neurosciences.

The second section is devoted to SQUID sensor technology addressing the main theoretical aspects and describing the design criteria of the different SQUID configuration relative to the realized device in view of their application to biomagnetic imaging. A shortly description of the fabrication process employed to realize all SQUID sensors is also given.

In the last section, a description of the SQUID based system for biomagnetic imaging of the brain is provided. The main parts are shown together with the testing of their effectiveness. Finally, the characterizations of the SQUID sensors, designed and fabricated, and a preliminary measurements to test the system effectiveness are reported.

Introduction to biomagnetism and relative systems

- **Introduction to Magnetoencephalography**

- **Biomagnetism: basic principle**

- **A simple model of bioelectric currents: the current dipole**

  - **The inverse prolem**

  - **Current-dipole solution**

  - **Lead field theory**

- **System architecture**

  - **Sensors**

  - **Dewar**

  - **Magnetic Shielding Room (MSR)**

  - **Data acquisition analysis**

  - **Meg Systems**

- **MagnetoEncephaloGraphy applicationsù**

  - **Neuroscience applications**

  - **Clinical Applications**

1.1   Introduction to Magnetoecephalography

The issue of the MagnetoEncephaloGraphy (MEG) is the measurement and analysis of weak magnetic fields generated by neuronal activity of the human brain [1]. It is broadly used both in advanced neurological and psychological research and clinical applications, to investigate brain functionality being a complementary but superior tool with respect to ElectroEncephaloGraphy (EEG). In particular, in most neurological and psychological studies, brain responses to various external somatosensory stimuli (auditory, visual, tactile, and olfactory) are measured [2]. The MEG is also successfully used in clinical application such as pre-surgical mapping, the epileptic foci location [3, 4], in the Alzheimer disease or to analyze post-stroke plastic reorganization of the brain subsequent to the ictus damages.

To locate effectively the activated areas, the results of such mapping have to be superposed with anatomical images obtained, usually, by Magnetic Resonance Imaging (MRI).

With respect to other brain functionality investigation tool such as Positron emission tomography (PET), functional Magnetic resonance imaging (fMRI) or Single-photon emission computed tomography (SPECT), the MEG has higher time resolution (3 order of magnitude) that allows to identify the whole activation sequence which is a fundamental requirement for instance in epilepsy study. Furthermore, MEG measurements are not distorted or attenuated by the insulating layer such as the skull, tissues or anatomical open spaces as in the EEG analysis. Finally, The MEG is a completely non invasive measurement requiring no contrast agent, magnetic field or x-ray.

1.2   Biomagnetism: basic principles

Biomagnetic fields are generated during the normal functioning of biological tissues which is managed by the exchange of ions (Na^+, K^+, Cl^-) between all

the excitable cells. The displacement of these ions originates the magnetic field. Here, the analysis is devoted to biomagnetic fields generated by the neuronal activity in the human brain, even the same issue may be applied to the fields generated by the heart activity or peripheral nerves.

The brain consists of about 100 billion cells of different type. Most of these are glial cells (astrocytes, oligodendrocytes, microglia) which are important for structural support, for proper ion concentration maintenance and for delivery of nutrients to the brain tissue. About 20 billions are neurons which are involved in the information processing and are electrically active.

Neurons can send electrical impulses, so-called action potentials, to other neurons nearby or to distant parts of the brain. They consist of a cell body (the soma), which contains the nucleus and much of the metabolic machinery, the dendrites, which are threadlike extensions that receive stimuli from other cells, and the axon, a single long fiber that carries the nerve impulse away from the soma to other cells.

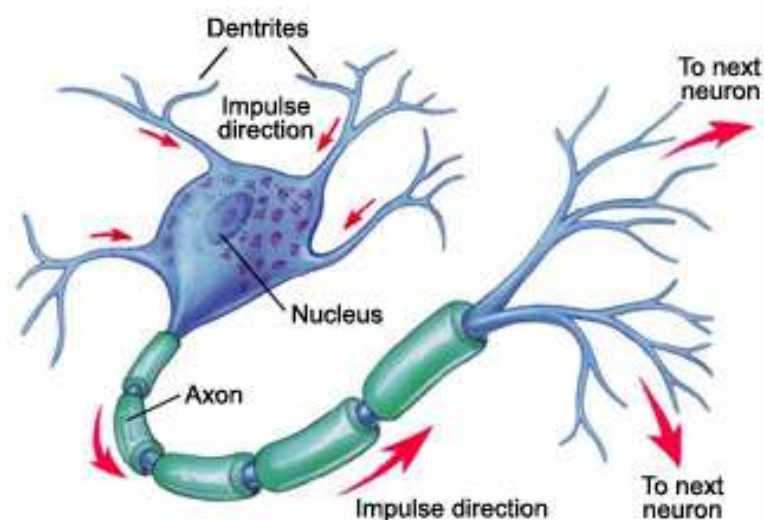Figure1.1 – Schematic representation of a neuron

The neurons are connected each to other by dendrites and to peripheral muscles and organs by axons. Both the axon and the dendrites terminate in a synapse that allows signal transmission by electrical or chemical means.

The dendrites and the soma have typically thousands of synapses from other neurons. The intracellular potential is increased by input through the

5

excitatory synapses, but decreased by inhibitory input. Most excitatory synapses are on the dendrites; inhibitory synapses often attach to the soma.

Since, the impulses are triggered at the synapse, the electrical potential are called postsynaptic potentials and consist in the sequence of a slow depolarization and a much slower repolarization that can last few tens of milliseconds and is the origin of most of the biomagnetic fields measured outside the human brain.

When a pulse arrives along the axon of the presynaptic cell, special transmitter molecules are liberated that perfuse the surrounding space sticking to receptors on the surface of the postsynaptic cell. As a result, the receptor molecules change their shape, opening ion channels through the membrane. Depending on the receptor which is activated, only certain types of ions may pass through the membrane. This flow of ions (Na^+, K^+, and Cl^-) is responsible of the membrane potential change in the second cell.
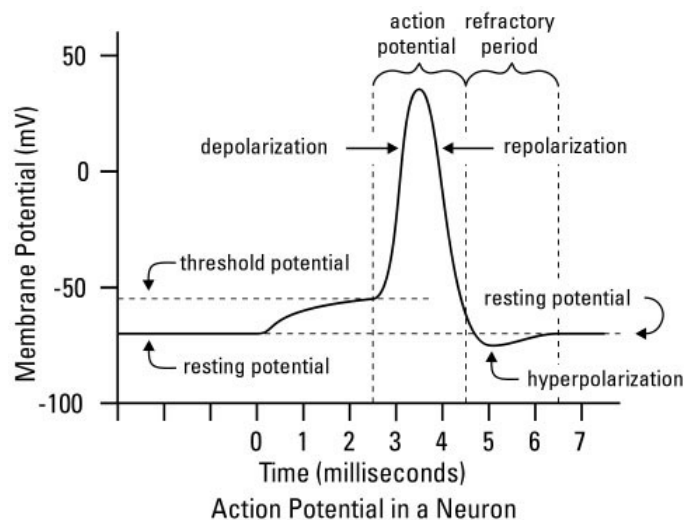
Figure 1.2 – The depolarization-repolarization sequence. The Na^+ ions inflow, thanks to open of relative channels, increasing the potential membrane up to 30 mV; subsequently, the K^+ channels are open allowing the outflow of these ions, restoring the starting potential.

There are various kinds of neurons, classified according to their shape and location within the brain:

- Stellate cells have a spherical symmetry with the dendrites that branch out in all directions.

- Cylindrical neurons that take up a cylindrical spatial domain in a perpendicular direction to the axons that passing through.
- Fan-shaped neurons (Purkinje's neurons) in which a single dendrite branches out from the main body still remaining in the plane to form a fan-shaped structure. These neurons, having up to 10^5 synapses, are mainly located in the cerebellum.
- The pyramidal neurons are relatively large; their apical dendrites from above reach out parallel to each other, so that they tend to be perpendicular to the cortical surface. Since neurons guide the current flow, the resultant direction of the electrical current flowing in the dendrites is also perpendicular to the cortical gray matter

Generally, the magnetic field **B** and electrical one **E** can be calculated starting from the Maxwell's equations [6-8]:

$$\nabla \times \vec{E} = -\frac{\partial \vec{B}}{\partial t} \qquad\qquad \nabla \cdot \vec{E} = \frac{\rho}{\varepsilon_0}$$

$$\nabla \times \vec{B} = \mu_0 \left(\vec{J} + \varepsilon_0 \frac{\partial \vec{E}}{\partial t} \right) \qquad \nabla \cdot \vec{B} = 0$$

And from the continuity equation.

$$\vec{\nabla} \cdot \vec{J} + \frac{\partial \rho}{\partial t} = 0$$

The time variability of bioelectric signals corresponds to a frequency range starting from dc up to a several hundred hertz.

Taking uniform the conductivity (σ) and considering the sinusoidal component of the signal at frequency f, the displacement current and ohmic one are it the ratio $2\pi\varepsilon f / \sigma$ which, using a typical brain values $\sigma = 0.25 \; \Omega^{-1}m^{-1} \; \varepsilon \cong 10\varepsilon_0$ and $f=100Hz$, assumes a value of 10^{-7}. At the same time, it can be demonstrated that the inductive effects become significant starting from a distance of several tens meters much higher than the head dimensions.

So, the explicit time-derivative terms in Maxwell's equations may be neglected and all the expressions of the field/potential due to electric current in the tissues may be therefore derived from the Maxwell's equation in the quasi-static limit:

$$\nabla \times \vec{E} = 0 \qquad \nabla \cdot \vec{E} = \frac{\rho}{\varepsilon_0}$$
$$\nabla \times \vec{B} = \mu_0 \vec{J} \qquad \nabla \cdot \vec{B} = 0$$

$$(1.1)$$

In addition, the charge conservation and Ohm's law can be taken in account:

$$\vec{\nabla} \cdot \vec{J} = 0 \qquad \vec{J} = \sigma \vec{E}$$

$$(1.2)$$

1.3   A simple model of bioelectric currents: the current dipole

To schematize bioelectric sources with a mathematical model, all contributions must be identified [9]. Neglecting the current through a membrane being small and radial directed, the involved currents can be divided into intracellular and extracellular ones.

The former, flowing from the resting region to the depolarization or the repolarization ones can be associated to the impressed currents J_i while the extracellular currents, closing externally the current loop between the depolarization and repolarization, can be associated to the volume currents $J_v = \sigma \cdot E$.

In particular, J_i can be schematized as a short oriented segment of current I and length L which is called current dipole as it generate a current distribution like to that one produced by a time dependent electrical dipole. It is characterized by a vector momentum, expressed in $A \cdot m$:

$$Q = I \cdot L$$

$$(1.3)$$

The relative current density function is given by:

$$J(r) = Q \cdot \delta (r - r_0)$$

$$(1.4)$$

where $\delta(r - r_0)$ is the Dirac delta function in three dimensions.

On the other hand, J_v represent the return ohmic current which guarantees the conservation of electric charge and must be considered when the magnetic field due to a current dipole is calculated. Since, the total current density in space due to a single current dipole is:

$$J = J_i + J_v = Q \cdot \delta (r - r_0) + \sigma \cdot E$$

$$(1.5)$$

The latter current flowing in the extracellular space is not physiologically related to neuronal activity.

The current dipole can be used as a model of elementary cellular events. Nevertheless, in the human brain a great number cells is involved in the signal processing, therefore, a macroscopic source may be modeled as an equivalent current dipole (ECD) by integrating the microscopic current distribution on the whole active region (*G*) [10].

$$\vec{Q} = \int_G J_i(\vec{r}')dv' \tag{1.6}$$

By using a current dipole, it is possible to solve the direct problem that is to calculate the magnetic field generated by a current dipole outside the head. By solving Maxwell's equations in the simplest case of an infinite homogeneously conducting medium, being σ constant everywhere in space, the magnetic field is:

$$\vec{B}_\infty(\vec{r}) = \frac{\mu_0}{4\pi} \frac{\vec{Q} \times (\vec{r} - \vec{r}_0)}{|\vec{r} - \vec{r}_0|^3} \tag{1.7}$$

Hence, the magnetic field due to a current dipole in an unbounded homogeneously conducting medium is generated only by active currents J_i. This results can be extended to a symmetric volume conductor in the case of a homogeneous spherical conductor [11], so the expression of the radial component of the field generated by a current dipole is given by:

$$\vec{B}_r(\vec{r}) = \frac{\mu_0}{4\pi} \frac{\vec{Q} \times (\vec{r} - \vec{r}_0)}{|\vec{r} - \vec{r}_0|^3} \cdot \hat{e} \tag{1.8}$$

where ê is the unit radial vector. In the neuromagnetic measurements, the head may be, on first approximation, considered as a homogeneous spherical conductor. Hence, the brain functionality is related to only the active current. In the case of more complicated geometry, like the real head, the above statement is no longer true and the volume currents play a role in the magnetic field generation which in this case, has no analytical expression and must be calculated numerically.

1.4 The inverse problem

The neuromagnetic inverse problem consists of the current source estimation which gives rise to a measured distribution of the magnetic field outside the head [12].

Unfortunately, the inverse problem is ill conditioned as a current distribution inside a conductor *G* cannot be retrieved uniquely starting from the measurement of the electromagnetic field outside.

Since there are primary current distributions that are either magnetically silent (*B=0* outside *G*) and/or electrically silent (*E=0* outside *G*), a solution obtained by adding one of them to a previous one represent still a solution. For instance, a radial dipole in a spherically symmetric conductor is magnetically silent but produces an electric field. To contrary, an example of an electrically silent current that produces a magnetic field is a current loop.

Due to non-uniqueness, to finding a solution the source configuration must be confined within a suitable constraints and small number of parameters have to be handled, so that the specification of the magnetic field at a sufficient number of points in space defines the source uniquely. Examples of such models are the single or multiple ECD, or the multipole expansion.

Alternatively, it is possible to assume a more complex source model imposing the constraints on the solution to make it unique that satisfies the prescribed criteria. In this case an array of a large number of current dipoles with fixed position is used as source model making linear the problem. Thus, only current calculation of dipole momenta is required.

1.4.1   Current-dipole solutions

Taking that, during a particular time interval, only one source is active, a single ECD may be a suitable source model. In this case, the magnetic field in the simplest approximation of a spherical volume conductor can be calculated by using the equation (1.8). Being in such spherical volume model the magnetic field generated by the two tangential components of the current dipole moment, only five parameters are needed to describe the model completely. These parameters (position and ECD moment components) can be obtained by a least-squares fit between the measured and the theoretical field values. Since, the dependence of magnetic field from ECD position is non linear, the suitable iterative procedures to best-fit parameters are needed [13,14]. The direct problem solution is iteratively calculated assuming for the

ECD coordinates, the current values of the corresponding parameters. In such a way, the parameter space dimension is reduced.

The validity of the fit may be evaluated by minimizing the residual:

$$R_{\min} = \sum_j \frac{(m_j - b_j)^2}{\sigma_j^2} \qquad (1.9)$$

Where m_j and b_j are, respectively, the measured and the theoretical magnetic field values at j-th sensor, σ_j is an estimate of the noise on this measurement. When two sources are simultaneously active and are close to each other or have extended field patterns which overlap, the source must be modeled by using a multiple ECD. The number of parameters involved increasing together with the complexity of the procedure [15]. To reduce parameters, fixed ECDs are used. In this case, the analysis benefit of the different time course of each different source. It can be used as additional information in conjunction with spatial one.

The basic assumption of this model is that there are several dipolar sources that maintain their position and, optionally, also their orientation throughout the time interval of interest. However, the dipoles are allowed to change their amplitudes in order to produce a field distribution that matches the experimental values.

The measured and predicted data may be expressed by the matrices M_{jk} and B_{jk}, respectively, where $j=1,...,n$ indexes the measurement points and $k=1,...,m$ corresponds to the time instants t_k under consideration. In this case the (1.9) becomes:

$$R = \sum_n \sum_m \left(m_{jk} - b_{jk}\right)^2 = \left\| M - B\left(x_1, \cdots, x_q\right) \right\|_F^2 \qquad (1.10)$$

where $x_1,...,x_q$ are the unknown parameters and $\| \ \|$ is the Frobenius norm. Since the residual depends nonlinearly on current dipole position parameters, the minimization of R entails an iterative search in parameter space. This requirement can be eliminated assuming that ECD positions are known on physiological grounds.

In this case the matrix containing the estimated time courses of the ECDs is given by:

$$Q_{est} = A^+M = \left(A^t A\right)^{-1} A^t M \tag{1.11}$$

where A is a transfer matrix and A^+ its pseudoinverse. Multiplying by A both members of (1.11) the projection of M onto the subspace spanned by the columns of A is obtained:

$$AQ_{est} = AA^+M = P_\parallel M \tag{1.12}$$

Thus, the minimized residual is given by:

$$R_{\min} = \left\| \left(I - AA^+\right)M \right\|^2 = \left\| P_\perp M \right\|^2 \tag{1.13}$$

where $P_\perp$ is the orthogonal projector.

An algorithm called MUSIC (multiple signal classification) simplifies the search for multiple sources [16]. The idea of the MUSIC algorithm is, once the number of current dipoles is decided, to find the best projector $P_\perp$ that minimizes (1.13) independently of matrix A. Then find the matrix A such that $(I - AA^+)$ best approximates $P_\perp$. Finally, find the current dipole moment time courses by using equation (1.11).

The best projector $P_\perp$ may be found by singular value decomposition of the data matrix M, while the matrix A is ideally orthogonal to $P_\perp$ and can be found by minimizing:

$$R' = \left\| A^t P_\perp \right\|^2 \tag{1.14}$$

1.4.2   Lead field theory

An alternative approach is to evaluate the magnetometer response to an arbitrary current distribution that is the basic of lead field theory [9].

Since, both magnetic and electrical fields are linearly dependent on J_i there is a vector field $\mathfrak{L}_i(r)$ such that (if m_i is the output of a magnetometer):

$$m_i = \int \vec{L}_i(r) \cdot \vec{J}_i(r) dv \tag{1.15}$$

The so-called lead field $\mathfrak{L}_i(r)$ describes the sensitivity distribution of ith magnetometer and depends on its coil configuration and on the conductivity σ.

The three components of $\mathcal{L}_i(r)$ correspond to the output of ith channel when a three unit current dipoles, displaced in r, points along the three direction of the coordinate system.

Similarly, if V_i is a potential difference between two electrodes, there is the corresponding electric lead field $\mathcal{L}_i^E(r)$ such that:

$$V_i = \int \vec{L}_i^E(r) \cdot \vec{J}_i(r) dv \tag{1.16}$$

The lead field can be obtained by computing the magnetic field $B=B(Q,r')$ generated by any dipole Q at any position r_Q.

This requires knowledge of the conductivity distribution so that the effect of volume currents can be properly taken into account. According with the equation (1.4), $\vec{J}_i(\vec{r}) = \vec{Q} \cdot \delta(\vec{r} - \vec{r}_Q)$ that entered into the equation (1.15) gives:

$$B_i\left(\vec{Q}, \vec{r}_Q\right) = \vec{L}_i\left(\vec{r}_Q\right) \cdot \vec{Q} \tag{1.17}$$

From which all three components of $\mathcal{L}_i(r)$ can be calculated for any r_Q.

If the magnetometer consists of a set of planar coils with normals n_j ($j=1,…,n$) oriented so that the winding sense is taken into account:

$$B_i\left(\vec{Q}, \vec{r}_Q\right) = \sum_{j=1}^{m} \int_{S_j} B\left(\vec{Q}, \vec{r}_Q\right) \cdot n_j dS_j \tag{1.18}$$

where S_j is the whole jth coil area. Therefore, a field such that $B \cdot n_j > 0$ produce a positive signal at the output.

Denoted as $\mathscr{F}$ the vector space of all square-integrable current distribution contained in a point set G inside the conductor, an inner product can be defined:

$$\left\langle J_1^i, J_2^i \right\rangle = \int_G \vec{J}_1^i(\vec{r}) \cdot \vec{J}_2^i(\vec{r}) dG \tag{1.19}$$

Then, from the equation (1.15), the output of the jth channel can be seen as the inner product of its primary current density and lead field, yielding information only about primary currents lying in the subspace $\mathscr{F}'$ spanned by the lead fields: $\mathscr{F}'=\text{span}(\mathcal{L}_1,…, \mathcal{L}_n)$.

In other words the component of J_i orthogonal to $\mathfrak{I}'$ is magnetically silent for our instrument and may not be retrieved from magnetic field measurements. So, the possible solutions to the inverse problem can be sought in the subspace $\mathfrak{I}'$. Such a solution J^s will therefore be a linear combination of the lead fields:

$$J^s = \sum_{i=1}^{M} \alpha_i L_i \qquad\qquad\qquad (1.20)$$

1.5   Systems for Magnetoencephalography

The measured magnetic field outside the head in typical conditions is, at most, 0.1 pT involving about 50.000 neurons. So, neuromagnetic fields are very weak fields compared to, for instance, the earth's magnetic field (about 50 μ T) or the field generated by electric power lines (about 10 nT). Slightly higher fields are generated by heart contraction (about 10 put). Furthermore the frequency content of the magnetic fields related to the functionality of brain ranging from the dc up to few hundreds Hertz. In the table 1.1, the intensities of some magnetic fields together with their frequency content are reported. It is evident that the biomagnetic field measurements must be performed by using a very good noise rejection technique.

Table 1.1 – Magnetic field amplitude generated by typical sources

Source	Amplitude (T)	Frequency range
MRI	1	DC
Earth	$50 \cdot 10^{-6}$	DC
Urban noise	10^{-7}	0.01Hz ÷ 1kHz
Hearth activity	10^{-12}	0.01Hz ÷ 50Hz
Brain activity	10^{-13}	0.1Hz ÷ 500Hz
Single neuron	10^{-18}	1Hz ÷ 1kHz

1.5.1   Sensors

On the basis of the above consideration, to detect a weak magnetic field a high sensitive sensor is required. The possible candidates are [2]:

Induction coil

The basic principle of the induction coil is based on the Faraday's law; i.e. in a conductive coil lying in a time dependent magnetic field, an electrical current is induced which increase proportionally with a turn number. The magnetic field can be evaluated starting from the current measurement. By using three orthogonal coils each magnetic field component can be detected. Unfortunately, being its sensitivity in inverse proportion to the field frequency, this tool is ineffective to measure static or low frequencies magnetic fields.
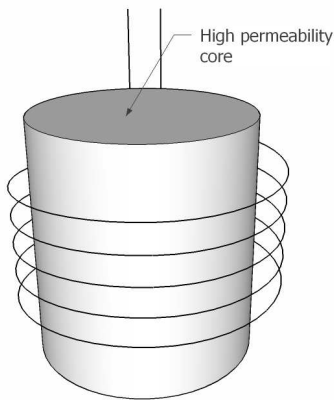
Fluxgate

A fluxgate magnetometer is a device that measures the intensity and orientation of magnetic lines of flux. The heart of the fluxgate magnetometer is a ferromagnetic core surrounded by two coils of wire in a configuration resembling a transformer. Alternating current (AC) is passed through one coil, called the primary, producing an alternating magnetic field that induces AC in the other coil, called the secondary. The intensity and phase of the AC in the secondary are constantly measured. When a change occurs in the external magnetic field, the output of the secondary coil changes. The extent and phase of this change can be analyzed to determine the intensity and orientation of the flux lines.
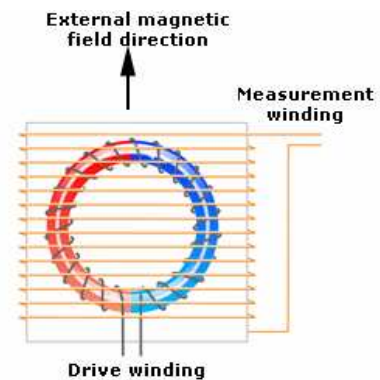
Superconducting Quantum Interference device (SQUID)

The SQUID is the most sensitive detector of magnetic field with an equivalent energy sensitivity that approaches the quantum limit [17]. Consisting of a superconducting loop interrupted by two Josephson junctions its principle of operation is based on the Josephson effect and flux quantization. When it is biased with a constant current the voltage output across it is a periodic function of the applied flux [18].
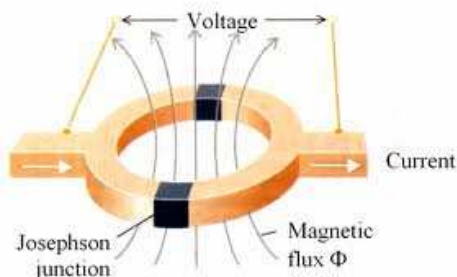
Optically pumped magnetometer

Remarkable field sensitivity has been demonstrated by a device that optically detects the change in the resonant condition of a gas of several atoms (rubidium, cesium or helium). An alternating field at ~400 Hz gives coherence to the orientation of the magnetic moments of optically pumped atoms, and the light they absorb or reemit is synchronously detected at this frequency with a lock-in amplifier. If the atoms sense a weak applied magnetic field, the resonant frequency is shifted and a change is observed in the intensity of absorbed or reemitted light. Field variations down to 200 fT could be detected even if in the case of simultaneous detection of the three components the sensitivity decreased by an order of magnitude. Optically pumped sensors are comparatively slow devices. Their bandwidths could be increased but at the expense of a reduction in sensitivity.

In the figure 1.3 the sensitivity of magnetic field sensors available are reported.
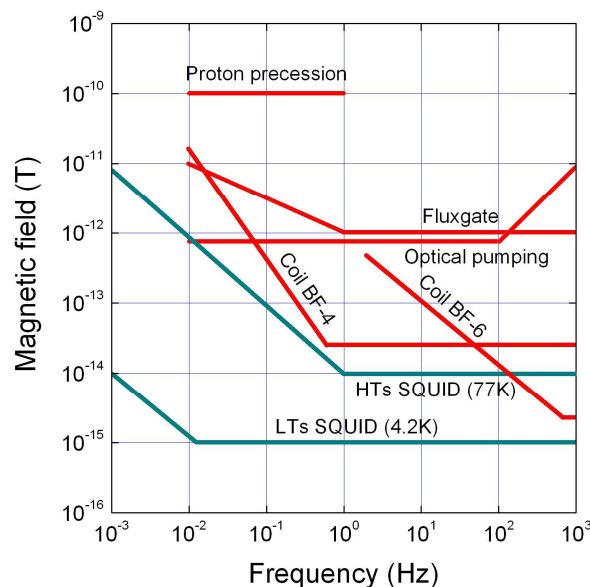
Figure 1.3 – Magnetic field sensitivity as a function of frequency of the most sensitive sensors

From the above consideration and taking into account that in the case of biomagnetic signals, most of the useful information for the clinical diagnosis is below 50 Hz, it is evident that, in this frequency range, the only sensor able to effectively detect the activity of the brain, is the SQUID with a low transition temperature [19], which will be addressed in detail in the next chapter.

So, a MEG system is based on SQUID sensors [20] that are arranged usually in a helmet shape to cover entirely the patient head. The sensors are immerged in helium bath to stay at T=4.2K by means of a Dewar. In figure 1.4 the scheme of MEG system base on SQUID magnetometer is reported.

Figure 1.4 – Schematic representation of a system for magnetoencephalography

1.5.2   Dewar

To keep the SQUID sensors at working temperature, a Dewar with high thermal insulation, is used. It is a container in which a high vacuum, in space between the inner and the outer shells, is realized to avoid thermal loss by the convection process.
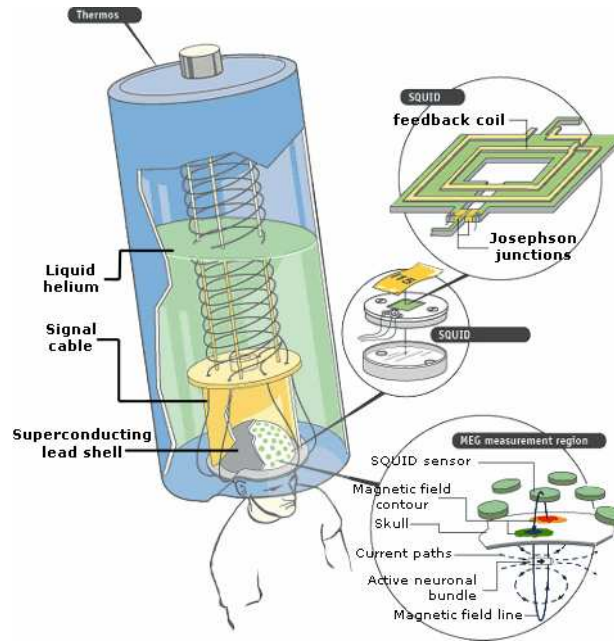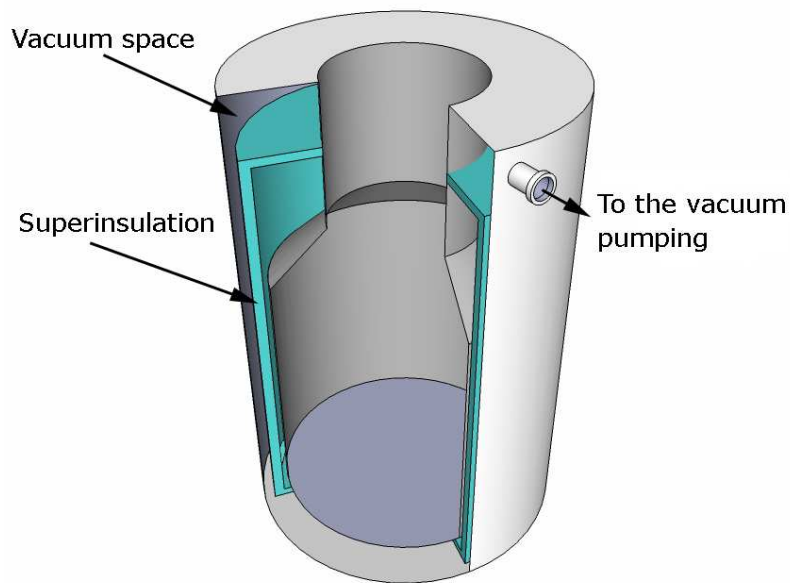
Figure 1.5 – Sketch of a Dewar for liquid helium.

To reduce the heat transfer by thermal radiation the vacuum space is superinsulated by using multiple layers of aluminized Mylar, or a comparable material having high reflectivity.

The Dewar for MEG measurements must be both nonmagnetic and electrically insulating.

Usually, due to their strength, insulating properties and low content of paramagnetic impurities, the fiberglass and plastics are elective materials to make a Dewar.

In the popular "vapor-cooled" Dewars the construction makes use of the cold evaporating helium to cool the space surrounding the innermost reservoir containing the liquid helium. Baffles force the gas to flow by the inner surface of the neck of the helium reservoir, and the neck in turn cools copper strips attached to the outer surface which run down to make thermal contact with the super-insulation at various points. The amount of super-insulation around the tail section, where the detection coil is located, must be kept to a minimum to avoid Nyquist field noise. The so-called "biomedical" Dewars of this type have been maintained with liquid helium continuously for periods of a year or more. Pellets of molecular sieve attached to the outer surface of the wall of the liquid helium reservoir serve to trap the small amount of gaseous helium that invariably leaks into the vacuum space over a long period of time. Dewars of this type depend on gravity to keep the helium in

the tail of the Dewar, so the axis of the Dewar must generally be kept within about 45° of the vertical. This is an undesirable limitation for many applications where it would be interesting to map the magnetic field at various positions around the body without moving the subject. A Dewar is best supported by wood or fiberglass, or other nonmetallic material that dampens vibrations.

1.5.3   Magnetic shielding room

The best way to reduce drastically both low and high frequency noise is to perform the measurements in magnetic shielding room (MSR) designed and realized on purpose.

The possibility to use a partial shielding especially designed to a portion of the body have been explored in the past, but such devices in addition to practical difficulties report noise level so far has been no better than can be achieved with a second-order gradiometer SQUID system in an urban laboratory. To contrary, a large room containing both the SQUID Dewar and subject is more effective and practical. Nowadays, most of the MEG systems work in owner "shielded rooms" designed on the basis of the noise condition at installation site.
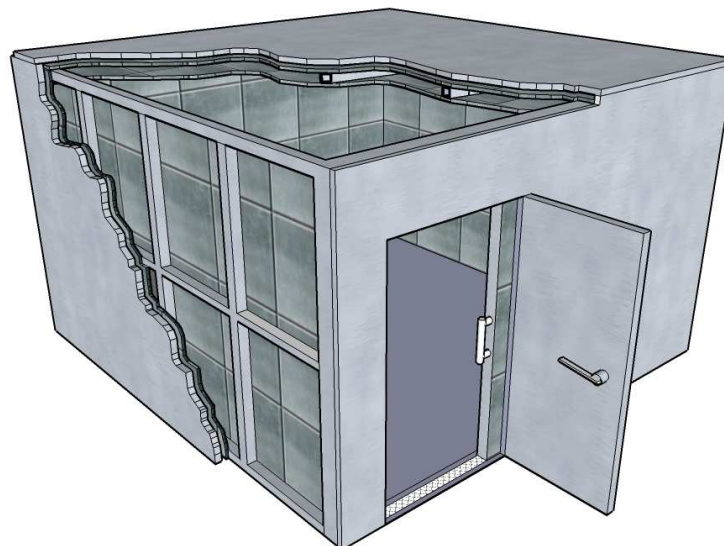

Figure 1.6 – Sketch of a magnetic shielding room in a typical cubic shape

It consist of several layer of high-permeability material for magnetic shielding in conjunction with one or more aluminum plates for additional eddy-current

shielding; in the latter, a time-varying magnetic field induces electrical currents that circulating in the aluminum layer generate a magnetic field which tends to cancel the changes of the applied magnetic field. The shielding efficiency is proportional to the frequency of the external magnetic field and depends on both the layer thickness and the conductivity of the materials.

At relatively low frequency (below 10 Hz), the eddy current shielding is no longer effective and shielding is provided by low hysteresis ferromagnetic materials with high magnetic permeability. Usually, a Fe–Ni alloy with small percentages of elements like Mo, Cu, Cr, or Al is used allowing to obtain a μ_r value as high as 10^4 H/m.

To improve the shielding factor a so called active compensation can be used [21]. It is achieved by feeding an appropriate current in a large Helmholtz-like coils wounded to the external perimeters of the MSR. The current value is calculated to minimize the residual magnetic field inside the room. Usually, this shielding technique is effective at frequencies lower than 1–2 Hz.

Typical MSRs have a cubic shape having a side length of about 3m and are built using two or three layers of μ-metal and one of aluminum having a thickness of about 20 mm located externally to at least one μ-metal layer to avoid the aluminum magnetic noise. The shielding factor increases with a number of μ-metal layers and with the distance between them. To minimize magnetic noise arising from vibrations, the room can be suspended pneumatically from the floor

The shielding factors of a typical MSR with a two μ-metal and one aluminum layers is about 55 dB at 1 Hz and 100 dB at 50 Hz.

If properly designed, a shielding room may reduce the residual magnetic field, at a frequency above 1 Hz, below the SQUID noise level ($\sim$5 fT/Hz$^{1/2}$). Below 1 Hz the noise increases with decreasing frequency.
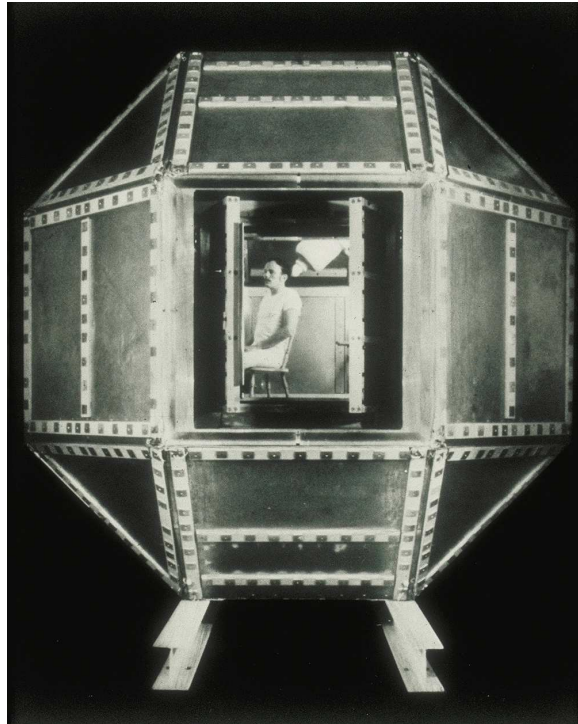
Figure 1.6 - The first magnetically shielded room for MEG built by David Cohen at MIT's Francis Bitter National Magnet Laboratory in 1969.

1.5.4   Data acquisition and analysis

All measurements are carried out by means of data acquisition systems therefore the signals has to be processed to match its amplitude and bandwidth to the dynamic range and sampling frequency of the analogue to digital converter (ADC) [22]. Due to high performance of digital filters, the analogical ones are used only for dc signals to avoid offset problems and for anti-aliasing low pass filter before AD conversion. For the latter requirement, the cutoff frequency must to be less than half of converter sampling frequency (f_s) and since its transfer function has non ideal shape, a frequency equal to $\frac{1}{4}f_s$ or $\frac{1}{3}f_s$ are typically chosen.

Furthermore, due to the large ADC dynamic range and the presence of environmental noise, a high pass filter may be required to avoid signal overflows. A first order high pass filter with a cutoff frequency as low as possible taking into account the ADC dynamic range, is employed.

As concern as the A/D converter a sampling frequency of 1 kHz is enough to process biomagnetic signals that have frequency less than few hundred Hertz.

Nowadays, very fast ADCs are available allowing to make a conversion by *oversampling* at a frequency up to 100 times the signal bandwidth. This technique allows for the filter to be cheaper because the requirements are not as stringent, and also allows the anti-aliasing filter to have a smoother frequency response, and thus a less complex phase response.

For MEG measurements, the required ADC resolution is at least 16 bit corresponding to a dynamic range of 96.3 dB enough for the most application.

In practice, the resolution of a converter is limited by the signal/noise ratio (S/N ratio). If there is too much noise to the analog input, it is impossible to convert with accuracy beyond a certain number of bit resolutions. This occurs when the magnetic shielding is not very effective or the magnetometers rather than gradiometers are used. In such cases a higher resolution is required and A/D converters having 32 bit resolution (192.6 dB) are used.

After the A/D conversion, if the oversampling has been used the data have to be decimated to reduce the amount of sample. This can be done by simply keeping a sample every n samples. To avoid aliasing due to downsampling a digital low pass filter is used to reduce the signal bandwidth to be processed.

With respect to analogue filter, the digital ones can be reprogrammed via software on the same hardware; moreover it is possible to modify in real time the filters parameters obtaining adaptive filters. The main types of digital filters are FIR (Finite Impulse Response) and IIR (Infinite Impulse Response). The FIR filter has a linear phase and is always stable, whereas the IIR filter may be unstable and its phase is generally non linear. Nevertheless if the phase distortion is tolerable, IIR filters is preferred because they involve a smaller number of parameters corresponding to lower computational complexity.

The FIR filters are easy to implement but require a large calculation number. The IIR filters use a feedback technique to hardly reduce the parameter number and their implementation is more difficult. In order to reduce costs and avoid possible instability, the most used filters are FIR type.

The use of Digital processing ensures good electronic noise rejection, since no valuable scattering in the performances of the different channels, especially concerning frequency-dependent time delays and sampling skew or jitters. In

addition, it is possible to build 'virtual sensors' or to perform electronic noise subtraction. Last, the on-line data handling makes it possible to monitor the signals and to perform some simple but useful data analysis, such as averaging, in order to check the correctness of the incoming data.

Once the data is collected, they have to be analyzed by suitable and user-friendly software to provide the results in a short time. The final results consist of the current density calculation starting from the measured magnetic field that is related to the brain activity.

The data analysis can be divided into two steps: At first from the magnetic field recorded by each sensor, the spurious magnetic field due to both sensor noise and unwanted sources must be reduced as low as possible; then, the current distribution can be calculated using a "cleaned" magnetic field by solving the inverse problem.

1.5.5   MEG Systems

Modern MEG systems are, as a rule, whole-cortex SQUID arrays measuring locally the radial magnetic field components of the brain [23]. The arrays of SQUID sensors are configured in helmet-shaped Dewars surrounding the scull which is usually suspended in a movable gantry for a supine or seated patient position. The present generation of Dewars contributes about 2 to 3 fT/$\sqrt{\text{Hz}}$ noise and limits the sensitivity of shielded MEG systems. This noise is generated by thermal fluctuations in various conducting materials in the Dewar vacuum space. The typical number of sensors ranges between about 120 and 300, and tends to be higher in the newest models. When combining shielding with high-order gradiometry and software denoising or spatial filtering, the system sensitivity can maintain that level in the signal bandwidth. Even if unshielded MEG operation is possible, research users usually require shielding for the best possible results. Usually, a large number of EEG channels is also included for simultaneous MEG and EEG data acquisition.
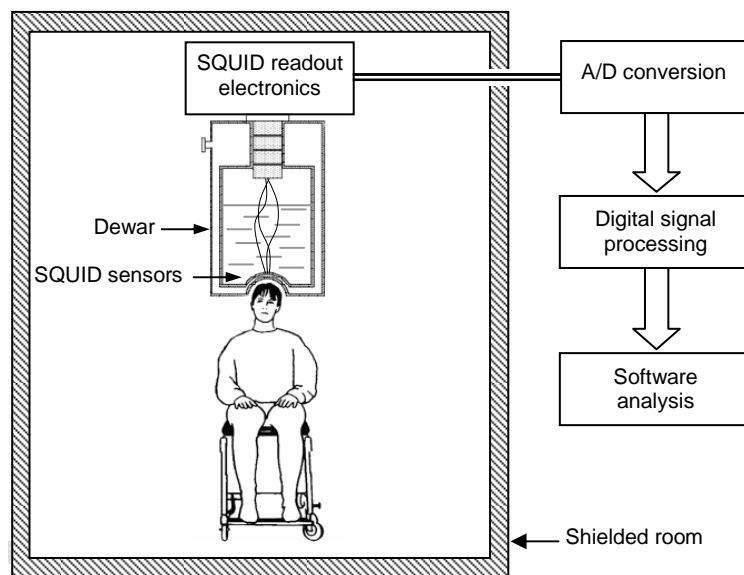
Figure 1.7 - Schematic block diagram of the MEG system

The SQUID system and patient are usually positioned within a shielded room. The MEG installations also have provisions for stimulus delivery and typically have an intercom and a video camera for observation and communication with the subject within the shielded room.

The electronics architecture provides for the management of large numbers of channels. It should be emphasized that even though the MEG signals are small, typically no more than about 1 pT, it is necessary to maintain a high dynamic range of the MEG electronics, due to the residual environmental noise within the shielded rooms, and, at lower frequencies, it can have a dynamic range as large as 20 to 22 bits for gradiometers and 26 bits for magnetometers. The SQUID flux transformers can be magnetometers, radial or planar gradiometers, or their combinations. The MEG sensor noise is usually range from 3÷10 fT/√Hz for radial gradiometer or magnetometers and about 0.3 fT/(mm·√Hz) for planar gradiometers.

The sensing coils are separated from the scalp surface by the vacuum gap in the dewar, which is typically 15 to 20 mm. References for noise cancellation, if present, are located some distance away from the primary sensors so that they detect the environmental noise, and are not sensitive to the brain signals. In the following, examples of some whole-cortex MEG systems are reported.

The CTF MEG system uses radial gradiometers with a 50-mm baseline as primary sensors and references suitable for noise cancellation by up to third-order synthetic gradiometers (29 references); the number of sensing channels is either 151 or 275. The Dewar orientation is adjustable between the vertical and horizontal positions.

The system uses a digital SQUID feedback loop with its dynamic range extended by utilizing the periodicity of the SQUID transfer function. The SQUID feedback loop is completed with digital integrator. With 304 SQUID channels (275 sensors and 29 references), up to 128 EEG, and 16 ADC, 4 DAC, and miscellaneous other channels, the maximum sample rate is 12 kHz.

The Magnes system of 4D Neuroimaging is pictured in Figure 1.9. The primary sensors are radial magnetometers, or axial gradiometers (with 50 mm baseline), or a combination of the two, with 23 remote references for noise reduction. The magnetometer flux transformers are mounted on the vacuum side of the liquid He reservoir. These systems can have either 148 or 248 sensors. The dewar is elbow-shaped and accomplishes the vertical and horizontal helmet positions by tilting in the range of −45° from the vertical. This system has 24-bit digitization with up to 8-kHz sample rates.

In the Elekta Neuromag system the sensor samples the neuromagnetic field by means of 204 planar gradiometers (baseline 17 mm), organized in orthogonal pairs, and 102 radial magnetometers centered on the midpoint of each planar gradiometer pair. Altogether 306 independent signals are thus acquired. The sensor components are made on a silicon chip using thin-film photolithography to provide a high degree of geometrical precision and balance.

The sensor combines the focal sensitivity of the planar detectors and the widespread sensitivity of the magnetometers in an optimal fashion. The system is also mounted in an elbow-shaped Dewar which allows a rapid change between sitting and supine position measurements. The maximum sample rate with 306 MEG and 64 EEG channels is up to 10 kHz and the signals are digitized to 24 bits.

A whole-cortex MEG system based on a superconducting imaging-surface concept (SIS–MEG) has been constructed and operated. The SIS-MEG consists of 149 low-Tc SQUID magnetometers surrounded by a superconducting helmet-like structure fabricated from lead. Sensors inside the helmet are shielded from environmental noise by 25 to 60 dB, depending on whether the sensors are close to the superconducting helmet brim or near the apex. In addition to the sensors, there are also four reference vector magnetometers (12 sensors) located outside the SIS helmet. The SIS almost completely shields the references from the brain signals, and the references are used in an adaptive noise cancellation approach to reduce the environmental noise. In addition to the passive shielding by SIS, the adaptive noise cancellation reduces the environmental noise by another 60 to 90 dB. Residual sensor noise is in the range from 2 to 10 fT/√Hz, depending on the sensor position relative to the SIS helmet.

1.6   MEG applications

The MEG is a powerful tool for biomagnetic imaging providing a great amount of scientific results stimulating a growing interest in both neuroscience and clinical applications. Actually, the MEG hold an important role in the field of functional imaging together with the functional magnetic resonance (fMRI), the positron emission tomography and single photon emission computed tomography (SPECT). With respect to the other diagnostics the MEG has a high temporal resolution of 1 ms which is a distinctive features if compared whit those of fMRI (1 s) or PET (1 min).

As concern as the spatial resolution, it depends strongly from signal-noise ratio and to data analysis features such as the accuracy of the source model or the volume. Nevertheless, the resolution ranges between 2 and 10 mm, than quite competitive with fMRI and PET having a spatial resolution of about 2mm and 2.5 mm respectively.

In the following, some of the most important achievements of MEG in basic neurophysiological and in clinical applications are briefly addressed.

1.6.1   Neuroscience applications

Spontaneous brain activity

Brain activity can be observed even in the absence of an explicit task, such as sensory input or motor output, and hence also referred to as resting-state activity [22]. Spontaneous activity is usually considered to be noise if one is interested in stimulus processing. However, it is considered to play a crucial role during brain development, such as in network formation and synaptogenesis. Furthermore this activity may provide information about the mental state of the person such as during the wakefulness or alertness and is often used in sleep research. Certain types of oscillatory activity, such as alpha waves, are part of spontaneous activity [24,25]. Statistical analysis of power fluctuations of alpha activity reveals a bimodal distribution and hence shows that resting-state activity does not just reflect a noise process.

Other examples of spontaneous activities are cortico-cortical and corticomuscular coherences just to mention a few.

Evoked activity

Somatosensory evoked fields (SEFs) are generated by stimulation of afferent peripheral nerve fibers by electrical means.

Typically, a square wave ranging from 0.2 to 2 ms duration is delivered to a peripheral nerve by surface electrodes. For intraoperative monitoring, needle electrodes are used for stimulation since they require smaller currents, which reduce the stimulus artifact. The usual sites for SEF stimulation are the median nerve at the wrist, the common peroneal nerve at the knee, and the posterior tibial nerve. A SEF also may be recorded by stimulating the skin in various dermatomal areas, but the response is much weaker.

It is possible to identify the different brain areas reacting to a sensory stimulus and to follow the propagation of the activation in a time window of about 200 ms. The low-level functions, namely primary functions, of the brain are very well defined from a spatial point of view, and, for instance, each section of the primary somatosensory area is dedicated to a specific body region with a spatially constrained feature.

The brain response to the stimulation of the left median nerve at wrist identifies a well defined source inside the primary somatosensory area, in the cerebral hemisphere contralateral to the stimulated side, followed by several other sources. The magnetic field can be recorded by one of the sensors together with the field distribution over the subject's head 21 ms after the delivery of the stimulus.

Follow the spreading of activation in time, the cerebral response at 100–130 ms latency, shows activation of two distinct brain areas in both hemispheres, corresponding to two secondary somatosensory areas [26]. As a comparison, if the same measurement is performed by a other functional imaging techniques, such as the fMRI, the cortical activation identifies active areas in the same districts but no time sequence of the activation can be inferred.

In the auditory evoked field (AEFs) with respect to tactile sensations, the sound characteristics are elaborated more intensely, both peripherally and centrally, before reaching our primary auditory cortex. In fact, the human ear is able to perform a frequency analysis before the sound vibrations are transduced into electrical signals and in addition the neural pathway includes

many synapsing relays before reaching the primary auditory cortex. MEG has been used largely to investigate the response of the auditory cortical regions to tone bursts or to temporally modulated stimulation demonstrating, in particular, the tonotopical organization within the auditory cortex [27].

In the visual evoked fields (VEFs) a even more sophisticated analysis of the spatial/intensity characteristics of light signals impinging onto the retina is performed before transmitting them to the primary visual cortex. MEG has shown both the retinotopic organization of the occipital primary visual cortex and variations of the retinotopy in nonprimary visual cortex [22]. Once again the temporal characteristics of the cortical activation are mandatory in understanding the perception of both simple visual pattern stimuli and motion.

Cognitive functions

Human sensorial systems transforms physical signals into electrochemical signals to our central elaborating regions, but also the sensory systems themselves perform high-level processing with discriminative abilities, which could be modulated significantly by attention. MEG has proven useful to investigate this issue, demonstrating, for instance, the auditory system ability in temporal discrimination and the relationship between primary cortical activity and perceptual systemic abilities [28].

Language function

MEG has a primary importance in the researches concerning language function which has great importance for human life. It is mandatory to understand how our mind works so as to develop both suitable teaching methods for students and rehabilitation procedures in pathological situations. The hemispheric laterality of the active brain areas during the language processing has been demonstrated. Different steps of language processing were focused on preattentive processing, discrimination between perception and recognition of word, between word or context comprehension, and comprehension of the whole sentence [29].

Physiological plasticity

Recent studies at cellular and systemic levels have shown human adult brain ability in modifying its functional activation properties in relation to modifications of peripheral or central homeostasis. In the short-term

timescale (less than few hours) it has been demonstrated that the cortical representation of one body district could invade the neighboring ones if the latter are deprived of their physiological sensorial input [30]. On longer timescales, central cortical representation changes have been observed in physiological conditions, as an effect of skillful movement learning: for example, simple sounds in the auditory cortical regions are more represented in musicians [31].

1.6.2 Clinical applications

Pre-surgical mapping

In order to minimize post surgical deficit on sensorimotor functionality, MEG measurements are performed to spatially identify the visual, auditory and motor cortex regions before any brain surgery. By using a high resolution anatomical imaging (i.e. MRI) the location of the functional primary areas can be indicate precisely in the individual stereotactic coordinate system. It has been also used to define a functional risk profile in the selection for surgery of a patient with brain lesions [32].

Usually this functional check is performed through electrocorticography, i.e. the measurement of electric potentials directly onto the exposed cerebral cortex, during surgery, thus increasing the time needed to complete the operation. While standard EEG is not accurate to a level useful for the surgeon, MEG has proven to be reliable in the identification of primary visual, sensory, motor, and auditory areas.

Identification of epileptogenic areas

MEG has proven to be of great usefulness in the study of the epileptogenic area in patients with partial epilepsy [33]. In these patients there is a restricted area of the brain that fires inappropriately, which can often be seen in an EEG as a set of sharp spikes. MEG analysis well localizes the epileptic foci by using the equivalent current dipole model. In patients whose disease is resistant to drug treatment, surgery may be used to remove the epileptogenic area. Its localization with the highest precision may limits as much as possible the amount of brain tissue surgically removed, thus reduces the risk of the patient being left with a permanent functional deficit.

Plasticity following central and peripheral lesions

The brain has no fixed organization, but the overall functioning is the result of an ongoing balancing between different 'inputs' from the periphery. Whenever there is a change from in homeostasis, the normal functioning is altered and usual brain functional architecture is promptly modified, at least to some extent. In particular reorganizations have been observed following partial deprivation of the sensorial inflow to the auditory system [34]. These abilities are of great importance as they subtend partially to the ability to recover after injury. Brain plasticity monitoring is useful, for instance, in the follow-up of patients recovering from a brain damage as vascular lesions, since the possibility of repetitive measurements during the rehabilitation phase may provide useful guidance for the assessment of the therapy.

Neurological dysfunction studies

Cerebral activity is altered in patients affected by neurological diseases with different etiologies, and some new insight could clarify subtending mechanisms. Alzheimer's disease is a pathology with growing social and economic impact, especially with the aging of the population. This disease has been studied by means of MEG to relate metabolic, anatomical and neurophysiological alterations.

In stroke patients, not only plastic effects, but also significant excitability alterations have been observed in both the affected and unaffected hemispheres [35].

Bibliography

[1]   Cohen D, Magnetoencephalography: evidence of magnetic fields produced by alpha-rhythm currents, Science 161, 784 (1968).

[2]   Romani G L, Williamson S J, and Kaufman L, Rev. Sci. Instrum. 53, 1815 (1982).

[3]   Modena I, Ricci G B, Barbanera S, Leoni R, Romani G L and Carelli P 1982 Electroencephalogr. Clin. Neurophysiol. 54, 622 (1982)

[4]   Barth D S, Sutherling W, Engel J Jr and Beatty J, Science 223, 293 (1984)

[5]   Koester J, Principles of Neural Science 2nd edn, ed E R Kandel and H J Schwartz (Amsterdam: Elsevier) pp 49–57 (1985)

[6]   Gulrajani R M, Bioelectricity and Biomagnetism (New York: Wiley) (1998)

[7] Malmivuo J and Plonsey R, Bioelectromagnetism (New York: Oxford University Press) (1995)

[8] Titomir L I and Kneppo P, Bioelectric and Biomagnetic Fields. Theory and Applications in Electrocardiology, (Boca Raton, FL: Chemical Rubber Company) (1994)

[9] Hämäläinen M, Hari R, Ilmoniemi R, Knuutila J and Lounasmaa O Rev. Mod. Phys. 65, 413 (1993)

[10] Katila T and Karp P, in Biomagnetism: an Interdisciplinary Approach ed S J Williamson, G L Romani, L Kaufman and I Modena (New York: Plenum) pp 237–63, (1983)

[11] Grynszpan, F., and D. B. Geselowitz, Biophys. J. 13, 911 (1973)

[12] Lima E, Irimia A and Wikswo J P, in SQUID Handbook vol II, ed J Clarke and A I Braginski (Berlin: Wiley–VCH) (2006), and references therein.

[13] Marquardt D W, J. Soc. Ind. Appl. Math. 11, 431 (1963)

[14] Nelder J A and Mead R, Comput. J. 7, 308 (1965)

[15] Scherg M, in Advances in Audiology Vol. 6, ed F Grandori, M Hoke and G L Romani (Basel: Karger) pp 40–69 (1991)

[16] Mosher J C, Lewis P S and Leahy R M, IEEE Trans. Biomed. Eng. 39, 541 (1992)

[17] Carelli P, Castellano M G, Torrioli G and Leoni R, Appl. Phys. Lett., 72, 115 (1998)

[18] Clarke J., A. Braginski, in The SQUID handbook, vol.1 Wiley-VCH (2004)

[19] Zimmerman J E, Thiene P, and Harding J T, Appl. Phys. 41, 1572 (1970)

[20] Cohen D, Science 175, 664 (1972)

[21] Platzek D and Nowak H, Recent Advances in Biomagnetism ed. T Yoshimoto et al (Sendai: Tohoku University Press) pp 17–19 (1999)

[22] Del Gratta C, Pizzella V, Tecchio F and Romani G L, Rep. Prog. Phys. 64, 1759 (2001)

[23] Pizzella V , Della Penna S, Del Gratta C and Romani G L, Supercond. Sci. Technol. 14, R79 (2001)

[24] Steriade M and Llinas R R, Physiol. Rev. 68, 649 (1988)

[25] Hari R and Salmelin R, Trends Neurosci. 20, 44 (1997)

[26] Hari R, Karhu J, Hamalainen M, Knuutila J, Salonen O, Sams M and Vilkman V, Eur. J. Neurosci. 5, 724 (1993)

[27] Romani G L, Williamson S J and Kaufman L Science 216, 1339 (1982)

[28] Sams M, Kaukoranta E, Hamalainen M and Naatanen R, Psychophysiology 28, 21 (1991)

[29] Helenius P, Salmelin R, Service E and Connolly J F, Brain 121, 1133 (1998)

[30] Rossini P M, Martino G, Narici L, Pasquarelli A, Peresson M, Pizzella V, Tecchio F, Torrioli G and Romani G L, Brain Res. 642, 169 (1994)

[31] Pantev C, Oostenveld R, Engelien A, Ross B, Roberts L E and Hoke M, Nature 392, 811 (1998)

[32] Hund M, Rezai A R, Kronberg E, Cappell J, Zonenshayn M, Ribary U, Kelly P J and Llinas R, Neurosurgery 40 936 (1997)

[33] Barth D S, Sutherling W, Engel J Jr and Beatty J, Science 218, 891 (1982)

[34] Tecchio F, Salustri C, Thaut M H, Pasqualetti P and Rossini P M, Exp. Brain Res. 135, 222 (2000)

[35] Rossini P M, Tecchio F, Pizzella V, Lupoi D, Cassetta E, Pasqualetti P, Romani G L and Orlacchio A, Brain Res. 782, 153 (1998)

Section II

dc-SQUID sensors for biomagnetic imaging

- **The dc-SQUID**

- **dc-SQUID noise**

    o **White noise**

    o **Flicker noise**

- **The detection circuit**

- o **The magnetometer configuration**

- o **The gradiometer configuration**

- **Geometrical design**

- **SQUID readout electronics**

- **SQUID sensors for biomagnetism**

  - o **The fully integrated SQUID magnetometer**

  - o **The miniaturized SQUID magnetometer**

  - o **The fully integrated planar SQUID gradiometer**

- **Fabrication process**

2.1   The dc SQUID

SQUID is the acronym of *Superconducting QUantum Interference Device* and is a very high sensitive magnetic flux detector with an equivalent energy sensitivity that approaches the quantum limit [1-3]. Nowadays, its sensitivity is approached only by extremely complex and impractical sensors based on optical pumping.

In particular, low critical temperature SQUID magnetometers are able to detect values of the spectral density as low as 1 fT/Hz$^{1/2}$. Such sensors are widely used in several applications which require high magnetic field sensitivity. One of the most relevant applications of SQUID devices is in multichannel systems for biomagnetic imaging which requires the detection of the extremely weak magnetic field originating from human body. In particular the interest is mainly focused on magnetoencephalography (MEG) and magnetocardiography (MCG) which provide useful diagnostic tools of heart diseases or brain functionality. In the last years, due to the mechanical

robustness and good resistance to repeated thermal stress of SQUID devices based on niobium technology, the number of channel in MEG systems has considerably increased. Large systems containing up to five hundred sensors have been developed.

A dc-SQUID consist of a superconducting loop interrupted by two Josephson junctions [4-6], hence, it combine two physical phenomena proper to superconductivity: The Josephson effect and the flux quantization in superconducting loops.

As concern as the first one, this effect consist of tunneling of Cooper pair trough a thin insulating barrier separating two superconductors [7-8]. This supercurrent flows with a density up to 10^4 A/cm^2 showing no voltage across the junction. The voltage remains zero up to a critical value of current.

The equations that manage the Josephson effect are reported below [9-11]:

$$J = \frac{2K}{\hbar}\sqrt{\rho_S\rho_D}\sin\varphi = J_0\sin\varphi$$
$$\frac{\partial\varphi}{\partial t} = \frac{2e}{\hbar}V$$
$$\vec{\nabla}\varphi = \left(\frac{2e}{\hbar c}d\right)\vec{H}\times\vec{n}$$

(1)

Where: V is the voltage across the junction, J_0 is the critical current and φ the phase difference between the macroscopic wave functions of the cooper pairs relative to two superconductors. Furthermore, K is a coupling parameter, H is the total magnetic field and d the penetration depth.

Referring to the magnetic flux quantization, it states that the magnetic flux treading a superconducting loop can assume only integer values of the flux quantum (2.07·10^{-15} Wb) [12]. This effect leads, in the case of dc-SQUID, to the following fundamental equation:

$$\frac{\varphi_a - \varphi_b}{2} = \pi\frac{\Phi}{\Phi_0}$$

(2)

Basically dc-SQUID is a flux to voltage converter which, when a steady bias current higher than the critical one is applied, shows an output voltage that is a periodic function of the applied magnetic flux with a period of one flux quantum. They can measure all physical quantities that can be converted into

magnetic flux, like magnetic field, voltage, current, displacement or magnetic susceptibility.
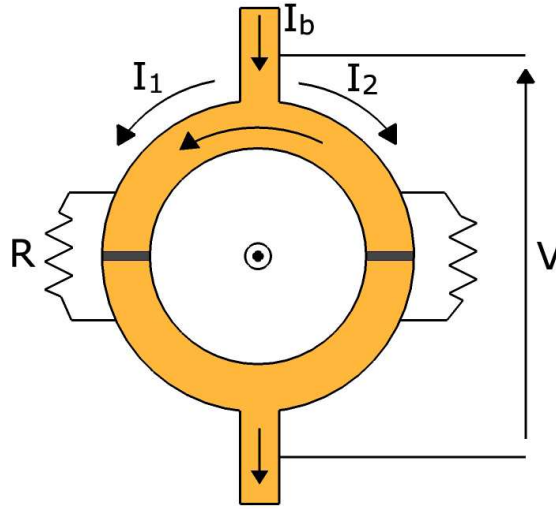

Figure 2.1 - Schematic representation of a dc-SQUID having shunted Josephson junctions

Considering the sketch of figure 2.1, where the Resistively Shunted Junction (RSJ) model [13-15] is used and assuming that the capacitance can be neglected, that is the Stewart-McCumber parameter $\beta_c=2\pi I_c CR^2/\Phi_0$ is much smaller than one, the transfer function has no hysteretic behavior.

Assuming that the two branches of loop are identical (same junctions then same critical current I_c, inductance L and resistance R) the analytical form of the $V\text{-}\Phi$ can be derived starting from the following equations involving the circulating currents in each branch and using the Josephson equation (1):

$$I_b = I_1 + I_2 = I_0 \sin\varphi_1 + \frac{V}{R} + I_0 \sin\varphi_2 + \frac{V}{R}$$

$$I_s = \frac{I_1 - I_2}{2} = \frac{I_0 \sin\varphi_1 - I_0 \sin\varphi_2}{2} \qquad (3)$$

In which φ_1 and φ_2 are the phase relative to two superconductors.

The (3) can be written as:

$$I_b = 2I_0 \sin\left(\frac{\varphi_a + \varphi_b}{2}\right)\cos\left(\frac{\varphi_a - \varphi_b}{2}\right) + 2\frac{V}{R}$$

$$I_S = 2I_0 \cos\left(\frac{\varphi_a + \varphi_b}{2}\right)\sin\left(\frac{\varphi_a - \varphi_b}{2}\right)$$

That using the equation (2) and setting $\varphi = (\varphi_1 + \varphi_2)/2$ become:

$$I = 2I_0 \sin\varphi \cos\left(\pi \frac{\Phi}{\Phi_0}\right) + \frac{2V}{R}$$

$$\frac{\Phi - \Phi_{ext}}{\Phi_0} = \beta_L \sin\left(\pi \frac{\Phi}{\Phi_0}\right) \cos\varphi \qquad (4)$$

Where $\Phi = \Phi_{ext} + LI_s$ and $\beta_L = 2LI_0/\Phi_0$.

If the inductance is negligible $\Phi \cong \Phi_{ext}$ and using (1)

$$I = I_c \sin\varphi + \frac{2}{R} \frac{\hbar}{2e} \frac{d\varphi(t)}{dt}$$

Taking $I_c = 2I_0 \cos\dfrac{\pi\Phi_{ext}}{\Phi_0}$

Solving the equation as in the RSJ model in the case of voltage state

$$\langle V(t) \rangle = RI_c \sqrt{\left(\frac{I}{2I_c}\right)^2 - \left[\cos\left(\pi \frac{\Phi_{ext}}{\Phi_0}\right)\right]^2} \qquad (5)$$

It can be seen that it is periodic with the applied magnetic flux having a periodicity of one flux quantum. Considering the time-averaged junction voltage as a function of the applied flux for different values of the bias current one can see that these curves are also periodic with the same periodicity. Furthermore, the minima and maxima of the $\langle V \rangle(\Phi_{ext})$ always appear at the same flux values. Furthermore, it is seen that the maximum modulation of the time-averaged voltage with varying applied flux occurs for $I \cong 2I_c$.

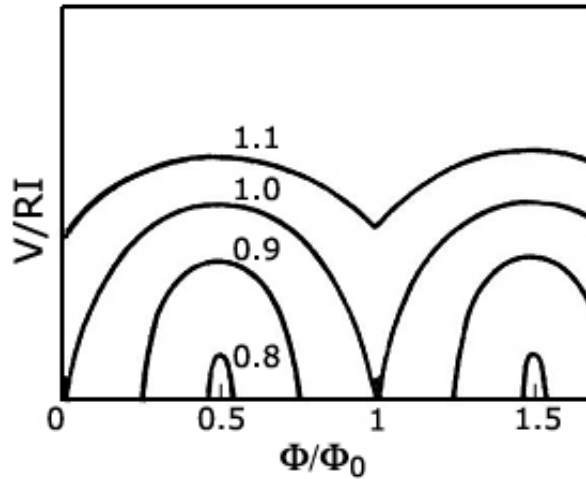In figure 2 some characteristic obtained by numerical resolution [6] are reported.

Figure 2.2 – External flux dependent voltage across a dc-SQUID

The dc-SQUID behavior in presence of a magnetic field makes it suitable as flux to voltage transducer, particularly when the very small flux changes have to be detected. To this aim, the working point should be set to obtain a transfer factor as high as possible:

$$V_\Phi = \left| \left(\frac{\partial V}{\partial \Phi_e} \right)_I \right| \tag{6}$$

In such a way, the output voltage is highest for a given magnetic flux change. Since the transfer factor (responsivity) corresponds to the angular coefficient of the tangent to the flux-voltage characteristic in its maximum slope point, as a first approximation it can be estimated as [16]:

$$V_\Phi = \frac{\Phi_0}{2} \frac{R_S}{L} \frac{1}{\Phi_0 / 2} = \frac{R_S}{L} \tag{7}$$

2.2   dc-SQUID noise

There are many noise sources that affect the SQUID sensitivity like the device intrinsic noise, that one arising in the pre-amplifying stages or the background noise. In any case, on output voltage across the SQUID can appear also if there is no input signal.

Thus, it is mandatory to estimate at least, the intrinsic noise level to achieve the bare sensitivity of the sensor.

The SQUID sensitivity is related to the magnetic flux power spectral density:

$$S_\Phi = \frac{S_V(f)}{V_\Phi^2}$$

where $S_V(f)$ is the power spectral density of the output voltage in absence of the input signal.

To compare dc-SQUID having different loop inductances, it is useful to refer to the energy spectral density per bandwidth unit:

$$\varepsilon(f) = \frac{S_\Phi(f)}{2L}$$

Such quantities show a typical behavior proportional to the reciprocal of frequency up to ~1Hz (flicker noise) then assume a constant value (white noise).

2.2.1   White noise

The white noise in a dc-SQUID is essentially due to a Nyquist noise produced by the shunt resistors of the junctions. A model for the calculation was provided by Tesche and Clarke [17] founding that white noise has low value when the thermal energy K_BT is much less than the Josephson one $I_0\Phi_0/2\pi$ that is:

$$\Gamma = \frac{2\pi k_B T}{I_0 \Phi_0} \ll 1$$

The minimum noise value is reached when $\Gamma=0.05$ and $\beta_L \cong 1$ (small thermal fluctuation regime) in this case, for the maximum responsivity, the following estimations are obtained:

$$V_\Phi \cong \frac{R}{L}$$
$$S_V \cong 16k_B TR \tag{8}$$
$$\varepsilon(\omega) \cong 9k_B \frac{TL}{R}$$

They are in good agreement with experimental data reported in literature.

2.2.2   Flicker noise

Often, to the SQUID the working at low frequencies is required. In this range there are different noise sources that affect a dc-SQUID.

One of them is the Josephson critical current fluctuations due to electron trapping and subsequent releasing in a defect of the barrier during a tunneling process [18-19]. This gives a local change in the potential barrier which produces a change in the critical current density. The mean time τ that the electron is trapped is an exponential function of activation energy and temperature and is distinctive for each trap. The current noise spectral density has a Lorentzian behavior:

$$S_{I_0}(f) \propto \frac{\tau_0 e^{\frac{E}{k_B T}}}{1 + (2\pi f \tau_0)^2 e^{\frac{2E}{k_B T}}}$$

The total one is obtained by integrating over all activation energy of the traps. Taking constant the bias current, the flux noise power spectral density at low frequencies can be approximated by [18]:

$$S_{\Phi}(f) \approx \frac{1}{2}\left[\left(\frac{\partial V}{\partial I_0}\right)^2 + L^2 V_{\Phi e}^2\right]\frac{S_{I_0}(f)}{V_{\Phi e}^2} \tag{9}$$

The first term is the so called "in phase mode" in which the junction fluctuations give an indirect contribution to the magnetic flux.

The second one represent the "out of phase mode", where the opposite fluctuations produce a circulating current in the superconducting loop resulting, directly, in a magnetic flux noise.
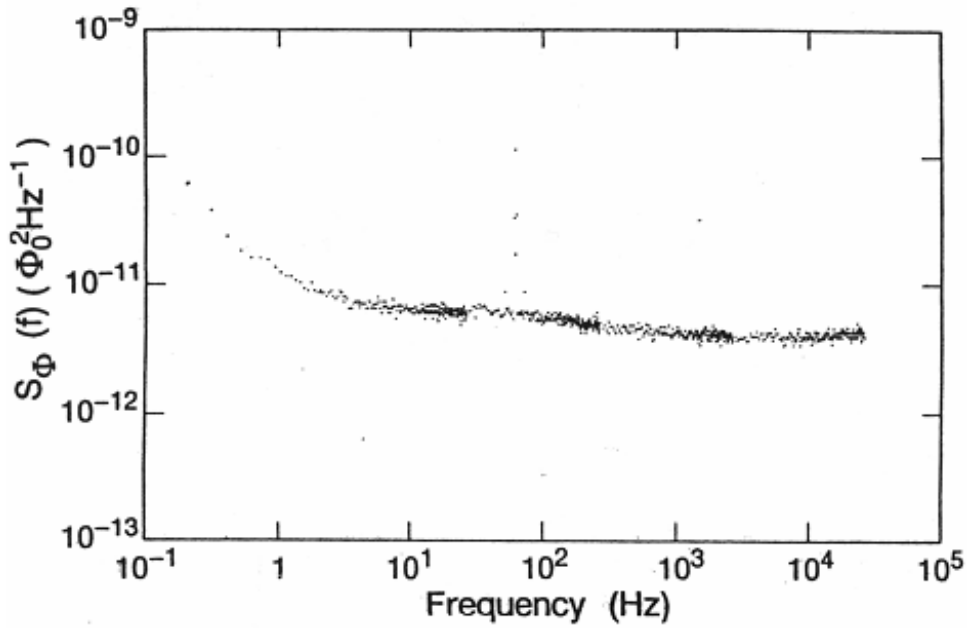
Figure 2.3 – Frequency dependent magnetic flux noise spectral density[1].

Another noise source is due to the random motion of Abrikosov vortices that appear as an additional external magnetic flux applied to the SQUID [19]. Its magnetic flux noise spectral density is proportional to the responsivity and is zero when V_Φ is zero.

2.3   The detection circuit

Since the dc-SQUID is a magnetic flux to voltage converter, its sensitivity is related to the flux capture area. Nevertheless, the sensitivity improvement cannot be obtained by simply increasing the SQUID superconducting loop dimension because this leads an increase of SQUID inductance and subsequent loss of performance as it can be seen by the equation (8)
Furthermore, the trapping energy of one flux quantum must be much more than the thermal energy, the SQUID inductance is limited by [19]:

$$L \leq \frac{\Phi_0^2}{5 k_B T}$$

At *T=4.2K, L* cannot be more than *15nH*
Usually, an efficient way to increase the sensitivity consists of using a proper detection circuit depending on the application.

In the case of the magnetic field measurement, as in the case of biomagnetism, the detection circuit is designed to measure magnetic field (magnetometer) or its gradient (gradiometer).

In both case, they consist of a series of pickup coil having a flux capture area much higher than the SQUID one, and an input coil inductively coupled to the SQUID loop.

2.3.1 The magnetometer configuration

Here, the flux transformer consists of a pickup circuit designed as a single coil, generally square shaped, connected in series with a multiturn input coil.
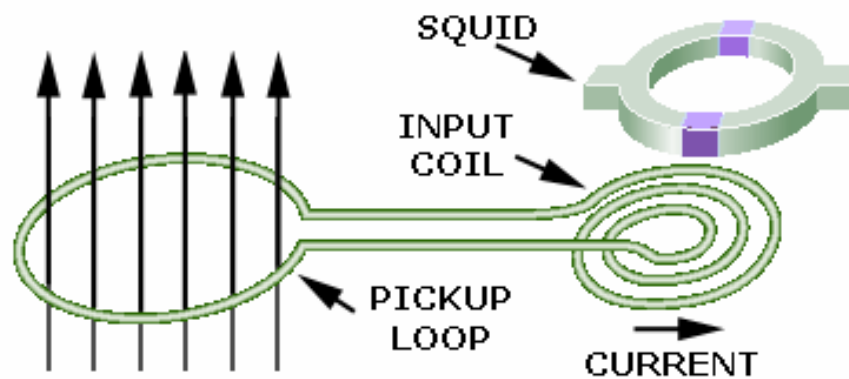

Figure 2.4 – Sketch of a magnetometer configuration

When a magnetic field is applied, due to Meissner effect, the relative flux generates into the pickup coil, a screening current to null the total magnetic flux. This current flowing in the input coil induces a magnetic flux into the SQUID loop [19]:

$$\Delta\Phi = \frac{M_i}{L_i + L_P}\Delta\Phi_p = \frac{k_i\sqrt{LL_i}}{L_i + L_p}\Delta\Phi_p \tag{10}$$

Where the input coil inductance and the pickup coil one have been indicated as L_i e L_p respectively; Φ_p is the applied magnetic flux, k_i is a coupling factor, and M_i is the mutual inductance between the SQUID loop and input coil.

In terms of equivalent flux noise:

$$S_\Phi^p = \frac{(L_p + L_i)^2}{LL_i}\frac{S_\Phi}{k_i^2} \tag{11}$$

That assume a minimum value when $L_p = L_i$.

To refer to magnetic field sensitivity, a magnetic field noise spectral density has to be considered which is related to a magnetic flux one by:

$$S_B^{1/2} = \frac{S_{\Phi,p}^{1/2}}{A_p} = \frac{L_p + L_i}{M_i A_p} S_{\Phi}^{1/2} = B_{\Phi} S_{\Phi}^{1/2} \qquad (12)$$

Here, A_p is the pick-up coil geometrical area. The conversion factor B_{Φ} from magnetic flux to magnetic field is a fundamental parameter for a SQUID magnetometer.

By using flux transformer an increase of field sensitivity of three orders of magnitude can be easily obtained with respect to the SQUID without flux transformer

2.3.2 The gradiometer configuration

To detect a magnetic field gradient a pickup coil of the flux transformer consists, usually, of two coils wrapped with the opposite direction. In order to evaluate the magnetic field gradient along the z direction ($\delta B_z/\delta x$) an axial configuration should be used [19], while for x or y dependent magnetic field gradient ($\delta B_x/\delta y$ or $\delta B_y/\delta x$) a planar configuration has to be employed [20].
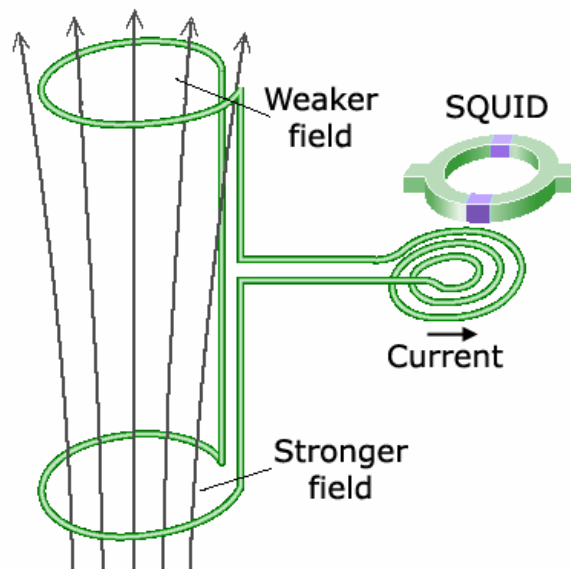

Figure 2.5 – Sketch of axial gradiometer configuration

In both cases, a spatially uniform magnetic field induces in the coils two screening currents having same amplitude but opposite direction, so that there is no current flowing into the input coil and subsequently there is no magnetic

flux treading the SQUID. If the magnetic field is non uniform the net current circulating into the input coil is non zero coupling a magnetic flux into the SQUID via mutual inductance M_i; in the axial case [20]:

$$\Phi_s = M_i J_s = \frac{2d^3 M_i}{2L_p + L_i}\left(\frac{\partial B_z}{\partial x}\right)$$

Where d is the distance between the pickup coil centers (baseline); thus the noise gradient is expressed by [20]:

$$\left.\frac{\partial B_z}{\partial x}\right|_n = \frac{2L_p + L_i}{M_i} = \frac{\Phi_n}{2d^3} \tag{13}$$

Here, Φ_n is the magnetic flux noise of the SQUID.

2.4   Geometrical design

Typically, the pickup coil consists of a single square shaped coil including, in one of its sides, a planar multiturn input coil which is located upper to the SQUID loop acting as a secondary coil of flux transformer [16,21-23]. A suitable SQUID loop design consists of a single coil having a square "washer" shape [24].
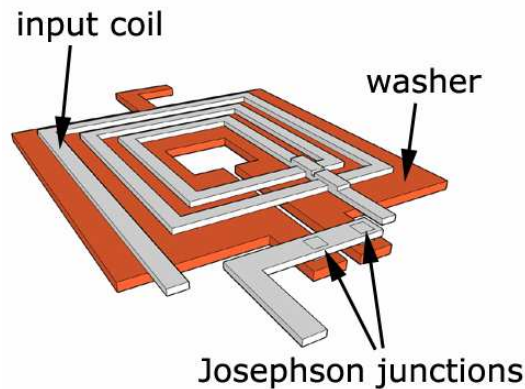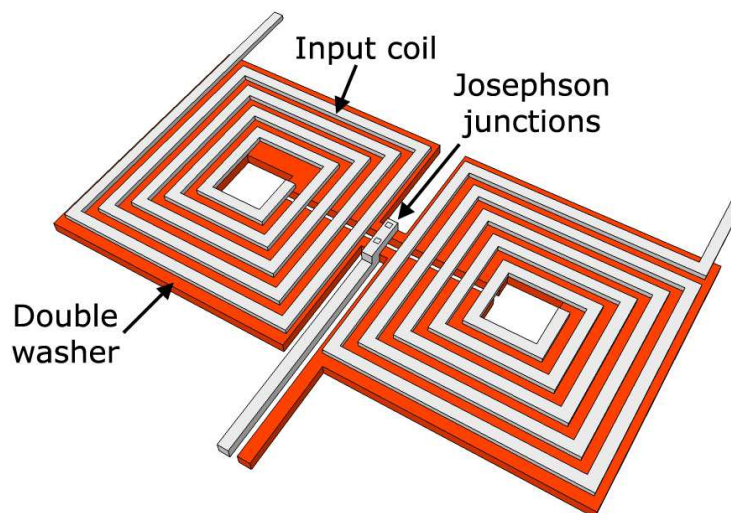

Figure 2.6 – Sketch of inductive matching between input coil and SQUID loop in a washer shaped configuration

In such a configuration, the current distributions are strongly thickened near the hole and falls rapidly toward the outer edge. If the outer dimension of the loop is changed, the current distributions are slightly perturbed.

So, the SQUID inductance does not depend on external dimension of the washer but only on the hole dimension.

The coupling between the washer and the input coil is very good and the input coil inductance is proportional to turn numbers and hole inductance. Hence, the input coil inductance can be adjusted to match a particular load by varying the outer dimension of the washer to accommodate the required number of turns in the input coil. The Josephson junctions are located on the outer edge of the square loop, away from the higher field region at the center square hole. As a consequence, a slit through the conductor loop is used, introducing excessive parasitic inductances. Such additional inductance is only partially coupled to the coil turns, reducing the overall coupling efficiency. So, it is preferable to avoid very long slit. Besides, the washer structure does tend to focus flux into the central hole by an amount proportional to the product of outer dimension D and the hole dimension d increasing the flux capture area by a factor given by the half of ratio between the washer area and the hole one. The flux focusing effect is largely employed to fabricate SQUID sensors for several applications.

Figure 2.7 – Sketch of inductive matching between input coil and SQUID loop in a double washer configuration

In the gradiometric configuration the input coil consists of two coils each one having n turns wrapped so that the screening current circulates in the opposite direction. The SQUID loop, still located under (over) the input coil to obtain

highest matching, consists of two washers, typically, in a parallel arrangement which allows obtaining half inductance with respect to a single washer. For it the same considerations of the single washer can be made.

2.5   The SQUID readout electronics

When a dc-SQUID are used as flux to voltage converter, the linear range corresponding to $(n+1/4)\Phi_0$ magnetic flux values of its characteristic is too small. To increase it a negative feedback circuit is used [25,26]. In such scheme, a voltage across the SQUID is amplified, converted in a current by a resistor and sent to a feedback coil inductively coupled to the SQUID loop generating, in the latter, an opposite magnetic flux to void the external one. The output voltage is measured across the resistor and it is proportional to the external magnetic flux.

This readout circuit is called Flux Locked Loop (FLL) and is often used when a high linear dynamic range is required.

In the direct coupled readout electronics, the dc-SQUID output voltage is processed by a low noise preamplifier and an integrator. Unfortunately, the noise contribution due to the amplifier is about one order of magnitude greater than the intrinsic SQUID one. Thus, the magnetic flux power spectral density is given by[24]:

$$S_{\Phi,t}(f) = S_\Phi(f) + \frac{S_{V,amp}(f)}{V_\Phi^2} \tag{14}$$

To use this scheme an increase of responsivity of, at least, one order of magnitude are needed.

To this aim an additional positive feedback (APF) circuit is used [25, 27]. It consist of a series of a resistor R_a and a coil L_a and acts so that a change in the output voltage, due to a change in the external magnetic field, produces a current in the APF circuit and subsequently an additional magnetic flux into the SQUID loop via the mutual inductance M_i resulting in an increase of responsivity which reduce a second term in the equation (14).

The APF produce an asymmetric change on the slope of the V-Φ characteristic; in particular, the slope increases at the working point while decrease on the opposite side

To avoid instability effect and a strong decrease of bandwidth, the APF gain should be less than one. Fortunately, a responsivity increasing of 20 times can be obtained for a gain value of about *0.95.*

Finally, including the APF circuit the magnetic flux noise spectral density is:

$$S_{\Phi,t}(f) = S_{\Phi,i}(f) + \frac{S_{V,amp}(f)}{|V_{\Phi}(f)|^2} + S_{I,amp}(f)M_{dyn}^2 + \frac{S_{V,a}(f)}{V_{\Phi,i}^2} \tag{15}$$

The terms of the above equation represent respectively: the SQUID intrinsic noise, the voltage and current noise sources and the Nyquist noise in the APF resistor. Typically, the current noise are small with respect to a voltage one and the last term can be reduced choosing a small value a APF resistor keeping a suitable current values into the APF coil.
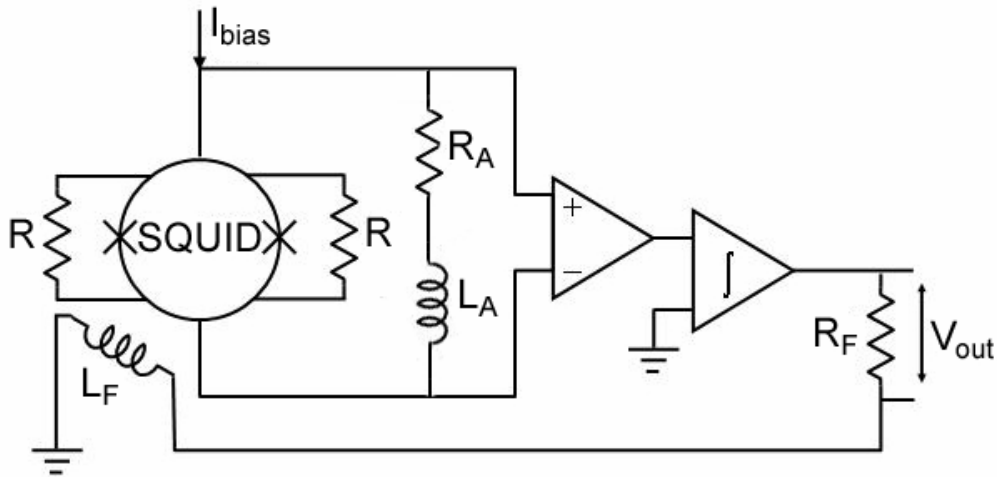

Figure 2.7 – dc-SQUID readout electronics including Flux Locked Loop and Additional Positive Feedback circuits.

To cover a large measurement area and improve spatial resolution, the SQUID base multichannel systems for biomagnetic imaging, can be contain up to five hundred sensors. In such systems crosstalk between neighboring channels could be a serious problem. It is essentially due to the spurious magnetic coupling existing between one pickup coil and the feedback coil of other sensors; the current flowing in a feedback coil to realize flux locked loop in a pertaining sensor induces a current also in the others. The crosstalk can be minimized by increasing the distance between the sensors to reduce the mutual inductance. Nevertheless, this is an impracticable solution in large

multichannel systems. An alternative method is to inject feedback current directly in the pickup coil so as the flux transformer current is nullified.

The crosstalk level due to feedback coil can be expressed as the ratio between the magnetic flux induced by a sensor in the neighboring one and in itself in a test sensor $\Phi_1 = \dfrac{\Phi_1^p M_i}{L_p + L_i}$ by a neighboring inducing one and the flux read by the inducing sensor $\Phi_2 = \dfrac{\Phi_2^p M_i}{L_p + L_i}$

$$\frac{\Phi_1}{\Phi_2} = \frac{\Phi_1^p}{\Phi_2^p} = \frac{M_{1,2}}{M_{1,1}} \tag{16}$$

Φ_1^p and Φ_2^p are the flux in the sensing coil of the two sensors, $M_{1,1}$ is the mutual inductance between the feedback coil and sensing coil of the inducing SQUID and $M_{1,2}$ is the mutual inductance between the feedback coil of the inducing SQUID and the sensing coil of the reading sensor. In order to reduce such a crosstalk, we have to minimize the ratio in the equation (16).

2.6 SQUID sensors for biomagnetism

Magnetometers and gradiometers based on superconducting quantum interference device SQUID are the elective sensors to employ in large multichannel systems for effective biomagnetic imaging.

A SQUID device in the magnetometer or gradiometer configuration should have both high magnetic flux sensitivity and a high flux to voltage conversion factor (responsivity). Here, the design criteria of different kind of fully integrated SQUID sensors for biomagnetic imaging based on niobium technology, designed, fabricated and characterized during the PhD period are reported.

In the gradiometer configuration, the SQUID washer inductance is reduced by using a parallel configuration which has half inductance with respect to single washer.

2.6.1   The fully integrated SQUID magnetometer

In the magnetometer a high sensitivity can be obtained by reducing the washer inductance keeping, at the same time, a suitable magnetic field to flux conversion factor B_Φ that depends on the pickup coil width.

The inductance of the washer is [16]:

$$L = L_{hole} + L_{slit} = 1.25\mu_0 d + L_T \cdot b$$

Where L_T is the slit inductance per length unit equal to *0.3pH/µm* by considering a two-dimensional slit and *b* is its length

For the flux transformer the inductance of pickup and input coils are [16]:

$$L_p = \frac{2}{\pi}\mu_0 D\left[\ln\left(\frac{D}{w_p}\right) + 0.5\right] \tag{17}$$

$$L_i = n^2\left(L_{hole} + \frac{L_T}{3}\right) + L_{strip}$$

w_p is the side width of pickup and D is its outer dimension; *n* is the turn numbers of the input and L_{strip} the parasitic stripline inductance; in this case the effective area of the pick-up coil, including the flux-focusing effect, is[16]:

$$A_p = D(D - 2w_p)$$

The mutual inductance between the input coil and SQUID is [16]:

$$M_i = k\sqrt{LL_i} \cong n\left(L_{hole} + \frac{L_{slit}}{2}\right) \tag{18}$$

Here k is a coupling constant which, in this design, is about 0.95.

An improvement in device performances has been achieved by increasing the flux capture area of the magnetometer. For such a purpose the mutual inductance between the input coil and the SQUID has been increased by a quite higher SQUID inductance. Due to the optimized design of both the SQUID and the pick-up loop, an effective flux-capture area of *3mm²* corresponding to a flux-to-field conversion efficiency of *0.7 nT/Φ_0* has been achieved [28]. Keeping $L_p = L_i$, k=1, using the previous expression and neglecting the stripline inductance, the B_Φ becomes [29, 30]:

$$B_\Phi = \frac{2\sqrt{\dfrac{2}{\mu_0} D\left[\ln\left(\dfrac{D}{w_p}\right) + 0.5\right]}}{D(D - 2w_p)\sqrt{L}}$$

In figure 2.8, the behavior of B_Φ as a function of the width w_p is reported taking the outer dimension of 8.2 mm. The minimum value of B_Φ corresponds to w_p value of about 0.56 mm. Nevertheless, a smaller value (0.2 mm) has been chosen to prevent flux trapping whose motion in the pickup loop body is a low frequency noise source. The resulting field sensitivity loss is less than *4%*.

The input coil structure may give rise to a variety of resonances, which can degrade the SQUID performance [5, 16]. To prevent it, the SQUID design has been optimized to move the resonance frequencies far from the SQUID operating one (f_{op}=0.3f_J), where $f_J = \dfrac{I_c R}{\Phi_0}$ is the Josephson frequency [16]. In addition, to avoid loss of performance due to a non optimal β_L value, a damping resistor across the SQUID loop has been inserted [31]. It also eliminates possible washer resonances guaranteeing smooth flux to voltage characteristics. The damping resistor value has been chosen equal to shunt of the junctions; in such a way a negligible change in the noise level with respect to the undamped SQUID is ensured.
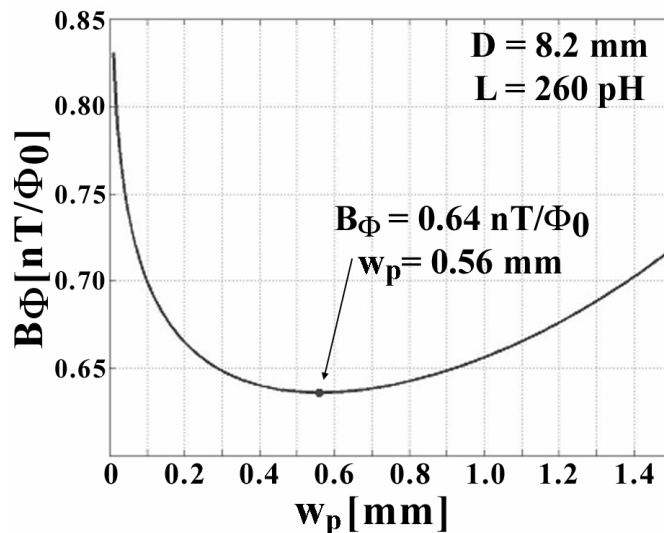

Figure 2.8 - *Flux to field conversion factor B_Φ as a function of pickup coil width for D=8.2mm and L=260pH.*

The peculiarity of this device consists of a fully integrated design including on the same chip the SQUID, the flux transformer, the FLL feedback coil and the whole APF circuit realized with a metallic film [28, 29].

Generally, the feedback coil consists of a single square coil, so a high desired mutual inductance between pickup and feedback coils $M_{1,1}$ implies a high undesired mutual inductance between the same feedback coil with a neighboring pickup one $M_{1,2}$. Here, a new feedback coil allowing to reduce mutual inductance $M_{1,2}$ and to increase the coupling with the pickup coil of the SQUID itself $M_{1,1}$ has been designed.

The increase of the $M_{1,1}$ also allows reducing a crosstalk due to the connection wires. The new design consists of two multiturn square coils wrapped so that the feedback current flows in opposite direction (Figure 2.9).
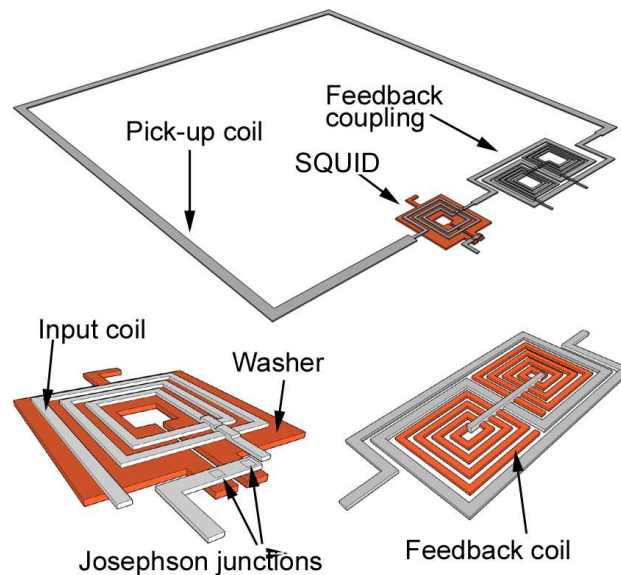

Figure 2.9 - Flux to field conversion factor B_Φ as a function of pickup coil width for D=8.2mm and L=260pH.

In such a way, as showed by simulations, the magnetic field outside the pickup loop decreases faster than a single coil. Each coil has an outer dimension of 150×150 μm^2 including 10 turns having both line width and turn spacing of 6 μm. The coupling between the feedback and the pick-up coils ($M_{1,1}$) has been maximized by using a properly pick-up loop in a eight-shaped configuration [29].
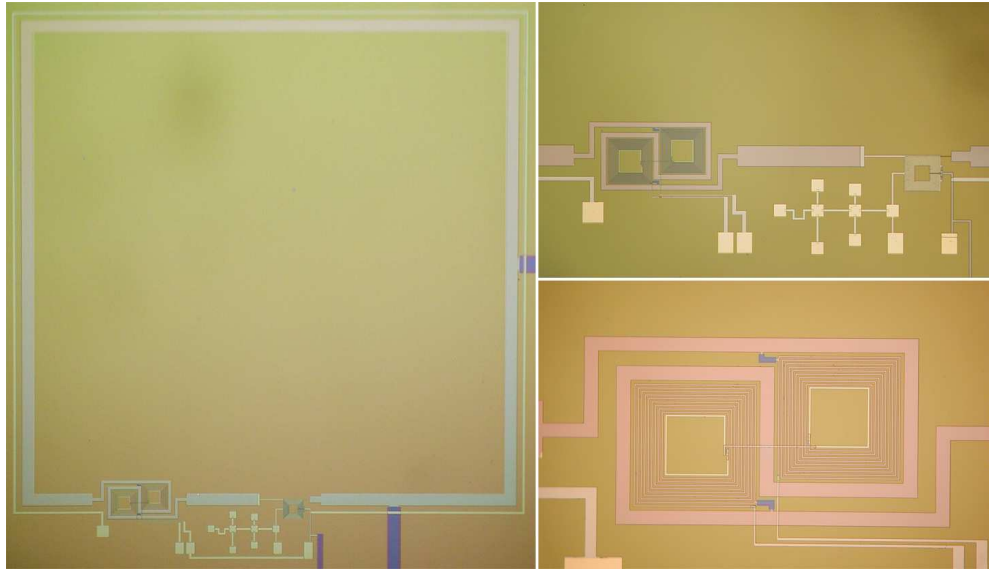
Figure 2.10 - Picture of the fully integrated SQUID magnetometer. On the right, the magnifications of SQUID washer, APF resistor set (upper), feedback coil and pickup coil arrangement (down) are shown[28].

Close to feedback the line width of pick-up loop is 50 μm while is 200 μm in somewhere else. The resulting flux-feedback current conversion factor is 11μA/Φ_0 comparable with the value obtained with a square feedback coil having an area 34 mm^2.

A bipolar feedback coil includes a resistive metallic film to avoid the resonant circuit L-C.

The APF coil, instead, having a square shape located outside the pickup coil has been made of a superconducting film. The possible resonances are damped by a suitable resistor selectable in a set of seven values ranging from 8 to 32 ohms. This offers also the possibility to change the APF gain to optimize the device performance.

In the table 1 main design parameters have been reported.

Table I : SQUID magnetometer design parameter

Josephson Tunnel Junctions			Pickup coil		
Critical current	$I_c = 10$ µA		Inductance	$L_p = 27$ nH	
Area	$A = 16$ µm^2		Side length	$D = 8.2$ mm	
Capacitance	$C = 1.3$ pF		Wire width	$w_p = 0.2$ mm	
Shunt resistance	$R = 3$ Ω		Effective pick-up coil area	$A_p^{eff} = 64$	
McCumber parameter	$\beta_c = 0.4$				
SQUID (washer)			Feedback coil		
Inductance	$L = 260$ pH		Feedback Inductance	$L_F = 94$ nH	
Hole dimension	$d = 140$ µm		Turn number	$n = 20$	
Outer dimension	$b = 390$ µm		Turn width	$w_F = 6$ µm	
Damping resistance	$R_d = 3$ Ω		Resistance of coil	$R \sim 180$ Ω	
Shielding parameter	$\beta_L = 2.5$		Mutual inductance**	$M_{F,P} = 4$ nH	
Input Coil			APF coil		
Inductance	$L_i = 33$ nH		APF Inductance	$L_F = 40$ nH	
Number of turns	$n = 12$		Turn width	$w_A = 20$ µm	
Wire width	$w_i = 4$ µm		Mutual inductance**	$M_{A,P} = 21$nH	
Wire pitch	$s_i = 4$ µm		APF resistor sheet	1.0 Ω/sq	
Mutual inductance*	$M_i = 2.9$ nH		Available values (seven)	8-32 Ω (step	

*With SQUID washer   **With pickup coil

2.6.2   The miniaturized SQUID magnetometer

To ensure the necessary magnetic field sensitivity for biomagnetic applications magnetometer having a sensing coil area of 60-70 mm^2 has to be employed. Furthermore, to obtain an accurate estimate of the magnetic field sources in the brain, together with their sequence of activation a large number of sensors is needed. Nevertheless, it is not possible increases the channel number beyond limit fixed by the surface area of the head or chest. Hence, in the large multichannel system the SQUID sensors are arranged very close each other over the measurement surface; it causes crosstalk problems and requires particular care for both wire arrangement and design of SQUID support, especially in system employing SQUID assembled in vacuum rather than in a liquid helium bath.

Therefore, to have a size-reduced SQUID magnetometer without loss of performance could be very useful.

The following design of a fully integrated magnetometer has been optimized to keep a suitable sensitivity. It has an area less than 10 mm^2 and includes a superconducting flux transformer, an additional positive feedback (APF) circuit and a bipolar feedback coil for low crosstalk operations [32]. The sensing

pickup circuit consisting of a superconducting square coil is connected in series with a 8-turn input coil, which is coupled to SQUID loop in a washer configuration. Apart from a better spatial resolution, a small pickup coil minimizes its antenna gain, reducing the effects of radio frequency interference. In order to improve the coupling properties between the SQUID and the input circuitry a SQUID with a large inductance (250 pH) has been used resulting in a rather large β_L parameters (~3.5). To prevent the degradation of the devices resolution the SQUID inductance has been shunted by a damping resistance equal to the shunt resistance of the Josephson junctions (γ = Rs/Rd =1). In fact, for a resistively damped SQUID, the responsivity and the voltage swing can be approximated by [32]:

$$V_\Phi = \frac{\partial V}{\partial \Phi} = 4 \frac{\alpha}{1 + \beta_{eff}} \frac{I_c R}{\Phi_0} \tag{20}$$

$$\Delta V = \frac{\alpha}{\pi} \frac{4 - \alpha}{1 + \beta_{eff}} I_c R \tag{21}$$

Where $\alpha = 1 - \sqrt{\beta_L \gamma}$, $\beta_{eff} = \frac{\beta_L}{\sqrt{1 + \beta_L^2}}$, $\gamma = \frac{2\pi k_B T}{I_c \Phi_0}$; $\beta_L = \frac{2 L I_c}{\Phi_0}$. I_c is the

critical current of the Josephson junction, R is the shunt resistance, C is the junction capacitance, and Φ_0 is the quantum flux. Note that β_{eff} approaches to 1 for large β_L, and consequently V_Φ of a large-β SQUID is comparable to V_Φ of a SQUID without R_d and β_L =1.

A relevant factor of merit for a SQUID magnetometer is the flux-to-field conversion efficiency inversely proportional to the effective capture area. In the case of a perfect match between the inductance of pick-up coil and input coil it is given by the (19); For this magnetometer design, setting D to *3 mm* and *L= 250 pH* the resulting w_p is again *0.2 mm* (see Figure 2.10). The other design parameters are listed in table 3. Note that the matching between the inductances of the pick-up and the input coil is not fulfilled. In fact, the length of the input coil has been increased with respect to the fit value in order to move away the resonance frequency of the input coil from the operating frequency of the SQUID. In any case such mismatch produces a very small

increase of the B_Φ (less than 10%). In order to reduce the equivalent preamplifier flux noise contribution with respect to the SQUID noise in the case of direct-coupled readout scheme an APF circuit has been integrated on the same chip. The integrated APF circuit includes a network resistor to adjust the APF gain for optimum device operation. The bipolar design of the feedback coil consisting of two multiturn coils allows to reduce crosstalk between neighboring sensors. An integrated thin film resistor (90 Ω) has been inserted in each multiturn coil in order to heat the device in the case of entrapped flux.
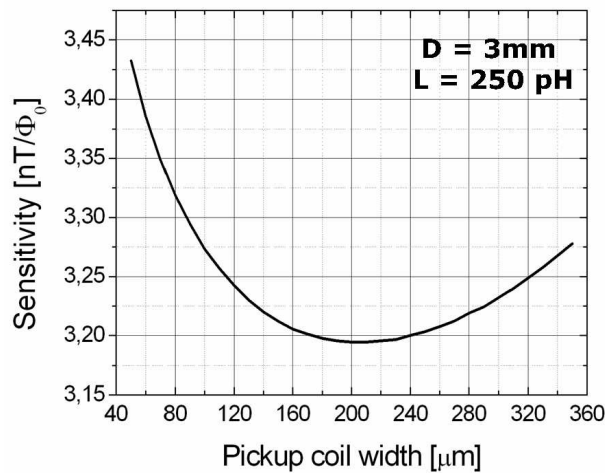
Figure 2.11 – Flux-to-field conversion efficiency of dc SQUID magnetometer as a function of pickup coil side width w_p for a perfect inductance match between the inductance of pickup coil and input coil.
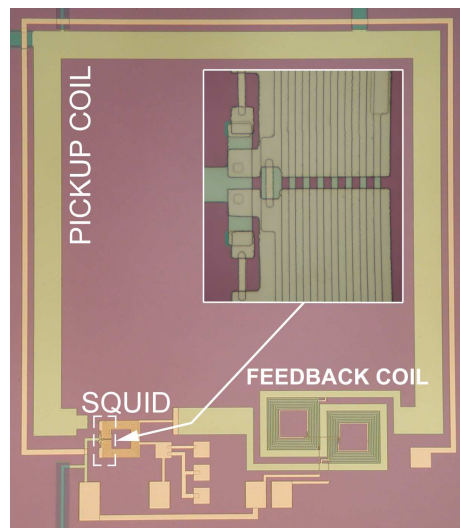

Figure 2.12 – Fully integrated SQUID magnetometer and a particular of Josephson junctions area [32]

2.6.3 The fully integrated planar SQUID gradiometer

Since background noise signals (~ 10 µT) exceed those of the biomagnetic sources by many orders of magnitude (1 fT-100 pT), both high shielded room and sophisticated noise cancellation techniques must be employed. Nevertheless, in order to obtain an acceptable signal/noise ratio either hardware (planar or axial) or electronic gradiometers are typically used. In the recent years, it is growing the interest for the first order planar SQUID gradiometers with a long baseline, which can be fabricated with intrinsic balance higher than the wire-wound gradiometers, thanks to the precision of the photolithographic techniques. Moreover, the pick-up loop inductance of a planar gradiometer can be well matched with the input coil's inductance ensuring a good signal coupling with the SQUID and the unreliable superconducting soldering are avoided. Due to the long baseline such sensors show a suitable sensitivity also to the deep biomagnetic sources. The simultaneous measurement of the two tangential components allows reducing the sensor coverage area necessary to get the essential magnetic field distribution, without loosing of the localization accuracy and the sensitivity.

The designed and realized sensor consists of a fully integrated first order planar SQUID gradiometer having a baseline length $d=50 \; mm$ [33]. A sketch of the device is shown in Fig. 2.9. The pickup antenna consists of two rectangular coils having an area of ($12\times10 \; mm^2$) and arranged in a series configuration which guaranteeing the absence of circulating current in whole pickup coil in presence of spatially uniform magnetic fields. Its total inductance L_p is given by the sum of the inductances of each coil and the relative interconnecting lines and is equal to 90 nH [33]. The collected signal is transferred to SQUID loop in a parallel double washer configuration via the inductive coupled input coil consisting of two windings of sixteen turns each. All inductance values, including the contributions of stripline and the washer slit are reported in the table II.

The sensor includes an integrated feedback coil for FLL operation, consisting of two multiturn coils (10 turns each), in a bipolar shape to reduce crosstalk between neighboring sensors. The coupling between the feedback and the pickup coils has been improved thanks to a suitable eight-shaped pickup coil

configuration (figure 2.13). In each coil, an integrated thin film resistor (90 Ω) has been inserted in order to heat the device in the case of flux trapping. The whole design has been optimized to avoid any drawing asymmetries in order to keep the expected balance level (1 part in 10000).
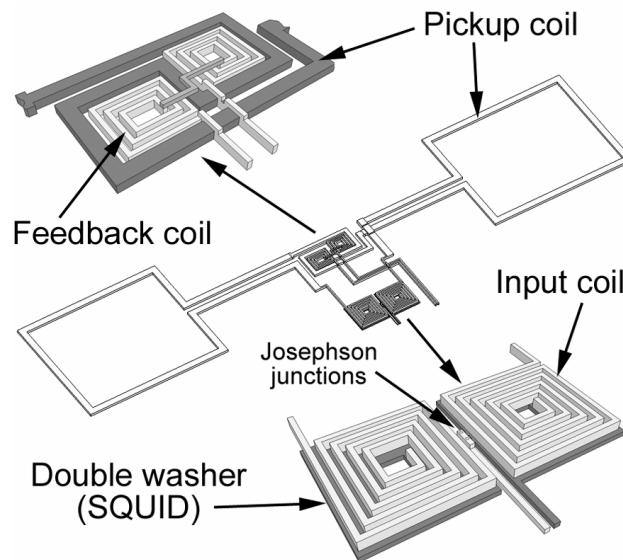
Figure 2.13 - A sketch of the first order planar SQUID gradiometer. The pickup coil, the parallel double SQUID washer and the bipolar feedback coil are shown.

The SQUID responsivity has been enhanced by increasing the critical current rather than the shunt resistor value that could lead to a more significant increase of β_C parameter because of its quadratic dependence from the resistance. In such a way, any additional readout circuit, like Additional Positive Feedback (APF), is needed avoiding unbalancing due to additional components.
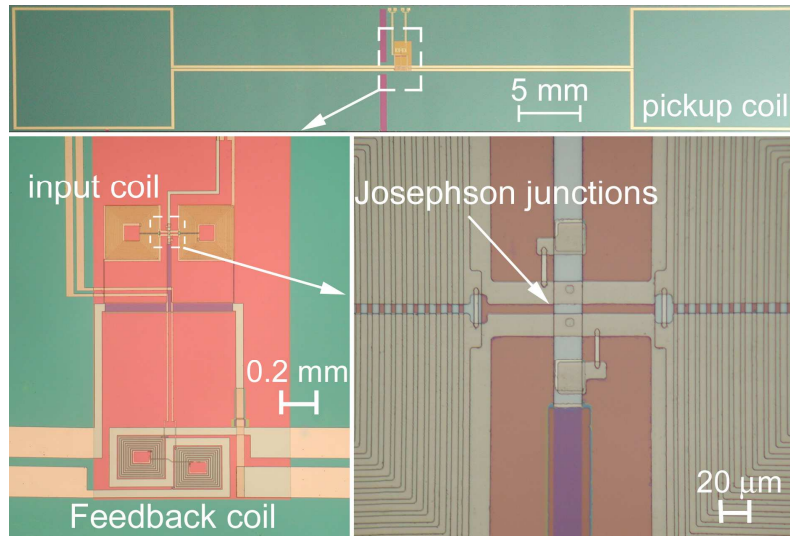
Figure 2.14 - Pictures of a fully integrated planar SQUID gradiometer. In the lower pictures the magnifications of feedback coil, double washer SQUID, input coil and Josephson junctions are shown.

It the table II, design parameter of the planar SQUID gradiometer are reported.

Table II: SQUID gradiometer design parameters

Josephson Tunnel Junctions		Pickup coil	
Critical current	I_c = 33 µA	Inductance	L_p = 90 nH
Area	A = 16 µm^2	Single coil area	D = 120 mm^2
Capacitance	C = 1.3 pF	Width	w_p = 0.2 mm
Shunt resistance	R = 3 Ω	Baseline	d = 50 mm
McCumber parameter	β_c = 0.5		
SQUID (washer)		Feedback coil	
Inductance	L = 130 pH	Feedback Inductance	L_F = 94 nH
Hole dimension	d = 100 µm	Turn number	n = 20
Outer dimension	b = 785 µm	Turn width	w_F = 6 µm
Damping resistance	R_d = 3 Ω	Resistance of coil	R ~ 180 Ω
Total slit length	l_s = 690 µm	Mutual inductance[**]	$M_{F,P}$ = 4 nH
Input Coil			
Inductance	L_i = 650 nH		
Number of turns	n = 80		
Wire width	w_i = 4 µm		
Wire pitch	s_i = 4 µm		
Mutual inductance[*]	M_i = 8.5 nH		

*With SQUID washer   **With pickup coil

2.6.4   Fabrication process

The Josephson junctions consist of two superconducting electrodes separated by a thin insulating barrier which can be obtained or by base electrode oxidation or by insulating film deposition.

Nowadays, a best way to obtain high quality LTc-junctions is to employ refractory materials having thickness of a few hundred nanometers; in particular, thanks to high gap value, the relatively high critical temperature and the robustness, the Niobium is widely used (Niobium technology [34-41]). To prevent lattice deformation or contamination, the thin films deposition is made in ultra high vacuum conditions.

Furthermore, by using the aluminum oxide artificial barriers with niobium electrodes, high quality and reliable junctions can be fabricated.

The realized sensors are based on niobium technology and Nb/Al-AlOx/Nb junctions are obtained by trilayer technique consisting of film deposition without breaking the vacuum.

The Nb/Al-AlOx/Nb trilayer is deposited by dc-magnetron sputtering on a oxidized silicon wafers (3″ diameter) and patterned by a lift-off technique. The trilayer is prepared in a thin film deposition station equipped with 2-inch-magnetron-sputtering sources and a rotary substrate carrier driven by a programmable stepping motor. The station is connected to a vacuum system consisting of a turbo-molecular and ion pumps. Before every process, the basic pressure is less than $4 \cdot 10^{-6}$ Pa. During the sputtering the argon pressure is maintained without any throttling. The base and the top niobium electrodes are deposited at a rate of 1.5 nm/s up to a thickness of 200 nm and 35 nm, respectively. The Aluminum layer, having a thickness of about 7 nm, is deposited at an effective rate of 0.09 nm/s, obtained by rotating the wafer carrier. The artificial (AlOx) tunnel barrier is obtained by thermal oxidation during 1-hour, filling the vacuum chamber with dry oxygen at a pressure of $2.5 \cdot 10^{4}$ Pa. The junction geometry (4x4 μm^2 window type) and the protection of the flux transformer are obtained by a standard photolitography and a Selective Niobium Anodization Process (SNAP). A further insulation is provided by a SiO_2 film (120 nm thick) deposited by rf-sputtering at a rate of 0.4 nm/s and patterned by a lift-off process. Shunt (R_s), damping (R_d), APF network and

heating resistors are obtained by an Au-Pd film deposited by dc-magnetron sputtering and defined by lift-off. Before the deposition, a buffer layer of molybdenum film (7 nm thick) has been deposited in order to improve the film adhesion. The sheet resistance of a 180 nm thick Au-Pd film, deposited at a rate of 1.5 nm/s, is resulted 1.5 Ω/sq at T=4.2 K. Finally, after an ion-beam cleaning process, a Nb film (500 nm thick), is deposited by dc-magnetron sputtering at a rate of 1.3 nm/s and then defined by a lift-off procedure. Such niobium film defines the junction contacts, the integrated coils, and the pads for electrical contacts. This procedure is capable to routinely produce window-type junctions having an area from (3×3) μm^2 to (100×100) μm^2 and exhibiting a quality factor V_m up to 80 mV. From the device testing a fabrication process yield of about 80% has been evaluated.

Trilayer deposition

Au-Pd resistor deposition

Junction definition by selective niobium anodization process and quartz deposition

Wiring

Top niobium removing by Reactive ion Etching (RIE)

- Niobium (Trilayer)
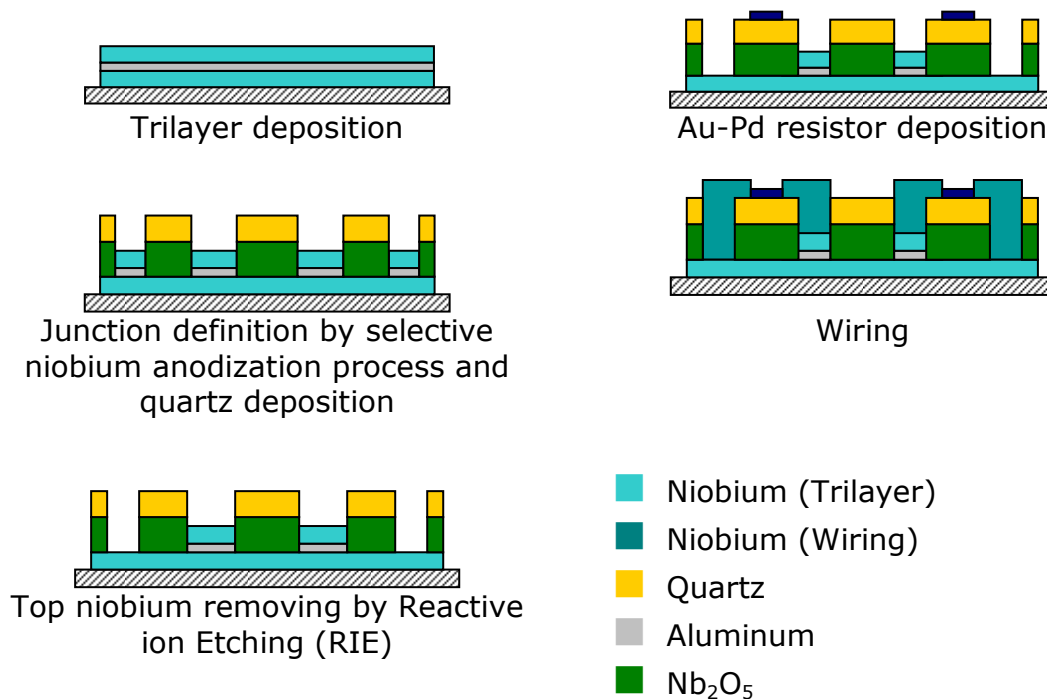- Niobium (Wiring)
- Quartz
- Aluminum
- Nb_2O_5

Figure 2.14 – Fabrication process outline

Bibliography

[1] J. Clarke, in Superconducting Electronics, NATO ASI Series F59, edited by H. Weinstock and M. Nisenoff (Springer, Berlin, 1989), p. 87. Clarke J., A. Braginski, in The SQUID handbook, vol.1 and vol 2 Wiley-VCH (2004 and 2006)

[2] Carelli P, Castellano M G, Torrioli G and Leoni R, Appl. Phys. Lett., **72** 115 (1998)

[3] Carelli, P; Castellano, MG, Physica **B**, **284,** 2039 **(**2000)

[4] Tesche C. D. and J. Clarke, J. Low. Temp. Phys., **29,** 859, (1976).

[5] Rynaen T., Seppa H., Ilmoniemi R. and Knutila J., J. Low Temp. Phys., **76**, 287 (1989).

[6] De Waele and De Bruyn R., Ouboter A. T. A. M, Physica, **41**, 225, (1969).

[7] Josephson B. D., Phys. Letters, **1**, 251 (1962).

[8] Josephson B. D., Advan. Phys., **14**, 419 (1965).

[9] Barone A. e Paternò G., Physics and Application of the Josephson Effect, Wiley Interscience ed. (1982).

[10] Solymar L., Superconductive Tunnelling and Application, Chapman and LTD, London (1972).

[11] Likharev K. K.: Dynamics of Josephson Junction and Circuits ; Gordon and Breach Ed., New York, (1986).

[12] Meissner W. and Ochsenfeld R., Naturwissenschoften, **21**, 787 (1933).

[13] McCumber D. E., J. Appl. Phys. **39**, 2053 (1968).

[14] Stewart W. J., Appl. Phys. Lett. **12**, 277, (1968).

[15] Fulton T. A., Phys. Rev. B **7**, 1189, (1973).

[16] R. Cantor dc-SQUID: design, optimization and pratical application", in SQUID sensors: fundmendals, fabrication and application, H. Weinstock Ed., Dordrecht: Kluwer Academic Publisher, (1996), pp.179-233.

[17] Tesche C. D. and J. Clarke, J. Low Temp. Phys. **27,** 301 (1977).

[18] Koch. R. H., Clarke J., Goubau W. M., Martinis J. M.,. Pegrum C. M and Van Harlingen D. J., J. Low Temp. Phys. **51**, 207 (1983).

[19] J. Clarke "SQUID fundamentals", in SQUID sensors: fundamentals, fabrication and application, H. Weinstock Ed., Dordrecht: Kluwer Academic Publisher, (1996), pp.1-62.

[20] Ketchen M. B., Goubau W. M., Clarke J. and Donaldson G.B., J. Appl. Phys. **44**, 4111, (1978).

[21] Ketchen M. B., IEEE Trans on Magn., **23** 1650-1657, (1987).

[22] Ketchen M. B., IEEE Trans. on magn. **27**, 2916 (1991).

[23] Jacox J. M. and Ketchen M. B., IEEE Trans. on magn., **Mag-17**, (1981).

[24] Ketchen M. B., Gallagher W. J., Kleinsasser A.W., Murphy S. and Clem J., in SQUID '85 Superconducting Quantum Interference Devices and Their Application Springer-Verlag Berlin, 865-871.

[25] D. Drung, "Advanced SQUID read-out electronics" in SQUID sensors: fundamentals, fabrication and application, ed H. Weinstock, (Dordrecht: Kluwer Academic Publisher, 1996, pp.63-116.

[26] Wellstood F., Heiden C. and Clarke J., Rev. Sci. Instrum. **55**, 952, (1984).

[27] D. Drung, R. Cantor, M. Peters, A. J. Scheer, and H. Koch, Appl. Phys. Lett., **57**, 406, (1990).

[28] Granata, C. Di Russo C, Monaco A, IEEE Trans. On Appl. Supercond., **11**, 95 (2001)

[29] C. Granata, A. Vettoliere and M. Russo, Appl. Phys. Lett, **88**, 212506, (2006). Vettoliere A, Granata C, Ruggiero B, Russo M, Int. J. Mod. Phys., B **23**, 5759 (2010).

[30] C Granata, A Vettoliere, M Russo, EUROCON, 2007. The International Conference on" Computer as a Tool", 556 (2007)

[31]   K. Enpuku, K. Yoshida, and S. Kohjiro, J. Appl. Phys., **60**, 4218, (1986).

[32] Granata C, Vettoliere A, Russo M, Appl. Phys. Lett., **91**, 122509 (2007).

[33] C. Granata, A. Vettoliere, C. Nappi, M.Lisitskiy, and M. Russo, Appl. Phys. Lett., **95**, 042502 (2009).

[34] Broom R.F.& al, IEEE Trans. on. Electr. Dev.,**27** ,1998 (1980).

[35] Gurvicth M.& al. Appl. Phys. Lett., **42**, 472 (1983).

[36] Gurvicth M.& al. IEEE Trans. on. Magn., **19**, 791 (1983).

[37] Imamura Fujistsu T. :Sci. Tech. **27**, 1 (1991).

[38] Kroger H.& al.: Appl. Phys. Lett., **39**, 280 (1981).

[39] Kroger H.& al.: IEEE Trans. on Magn. **19**, 783 (1983).

[40] Morohashi S. and Hausuo S., J. Appl. Phys., **61**, 4835, (1987).

[41] Morohashi S.& al.: Appl. Phys. Lett., **4**6, 1179, (1985).

The SQUID based MEG system: Design, characterization and preliminary measurements

- **Characterization of the SQUID sensors**

    o **The magnetometer**

    o **The miniaturized magnetometer**

    o **The planar gradiometer**

    o **The crosstalk evaluation**

- **The MEG system**

    o **The Dewar design and performance**

    o **The magnetic shielding room performance**

    o **System characterization and preliminary measurements**

3.1 Characterization of the SQUID sensors

The SQUID sensors have been characterized in liquid helium at T = 4.2 K shielded by a coaxial lead/cryoperm double can [1, 2].

In the following, the characterization of all sensors described in chapter 2 is reported. A readout electronics is based on direct-coupled scheme for the Flux Locked Loop. An amplifier voltage noise, as low as 0.5 nV/√Hz at 10 Hz has been obtained by inserting in front of the first amplification stage, a differential amplifier built around a PNP matched transistor pair (SSM2220) [3]. All of the electrical connections to room temperature were radio frequency filtered.

3.1.1 The magnetometer

As shown in the paragraph 2.6.1, the SQUID loop is a square planar washer with an inductance of 260 pH, coupled to a 12-turn thin film input coil with 33 nH inductance connected in series with a square single turn pickup coil of 64 mm^2 area and 0.2 mm width having an inductance of 27 nH [3-5].

In order to reduce to a negligible value the amplifier flux noise contribution, the APF circuit as been integrated on the same chip obtaining an asymmetry in the voltage-flux characteristics. The measured one is reported in figure 3.1 and it appears smooth and resonance free ensuring stable working operations at optimal point.
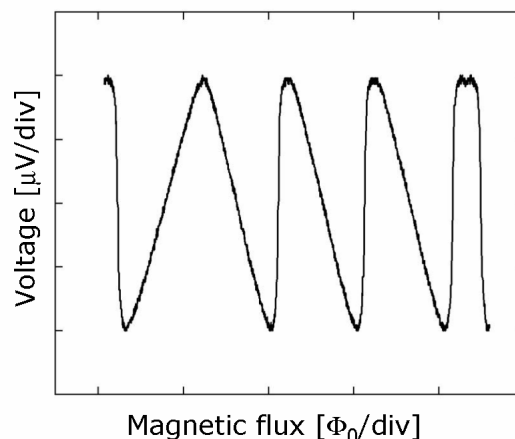

Figure 3.1 – Flux dependent voltage characteristic of the SQUID magnetometer

In the figure 3.2, the magnetic field and flux noise spectral densities are shown. In the white region of the spectrum, a value as low as 1.7 fT/√Hz has

been measured. The 1/f corner is essentially due to the low frequency noise of the amplifier. The linear dynamic range has been evaluated considering an electronic gain of 0.2 V/Φ_0 and a saturation threshold of 5V. If a properly electronic is used, it is possible to reach a slew rate value greater than 1 mT/s. The flux-to-field conversion efficiency B_Φ equal to 0.7 nT/Φ_0 has been measured by means of calibrated Helmhotz coils.

Note that:

- The measurements performed on the same samples using the external APF circuit and feedback coil has shown a significant increase of the magnetic field noise level confirming the effectiveness of the fully integrated configuration.

- Noise measurements performed on similar SQUID devices using a standard modulate electronic circuit have shown a typical 1/f behavior over more than 2 decades with a corner frequency below 1.5 Hz.

- The slew rate has been measured using a low noise read-out electronic in FLL configuration designed for biomagnetic measurements where it is not required to measure fast and high frequency signals. In Table II a summary of the experimental characteristics is presented
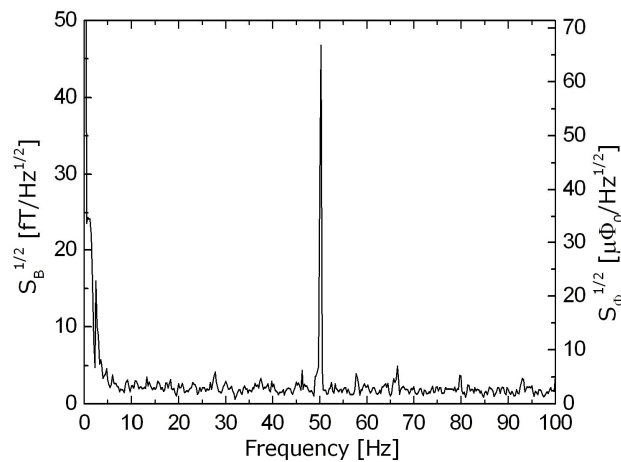

Figure 3.2 – Magnetic field (and flux) noise spectral density

Table I : Magnetometer performance

Voltage Swing	15-30 μV		Magnetometer field noise	1.7 fT/Hz$^{1/2}$
Critical current	15-25 μA		Slew rate (f>200 Hz)	6.6 μT/s
Intrinsic responsivity	50-100 μV/Φ_0		Linear dynamic range	2.3 x 10^7 /Hz$^{1/2}$
Field-flux sensitivity	0.7 nT/Φ_0		Energy sensitivity	4.0x 10^{-32} J/Hz
Effective SQUID area	3 mm^2		1/f corner	less than 3 Hz
Magnetometer flux noise	2.4 μΦ_0/Hz$^{1/2}$			

3.1.2   The miniaturized magnetometer

As shown in the section 2.6.2, it is a fully integrated device having a flux transformer area less than 10 mm^2. Despite the reduced dimensions it includes an APF circuit and a bipolar feedback coil for low crosstalk operations [6-8]. The sensing pickup circuit, consisting of a superconducting square coil with a length of 3 mm, is connected in series with a eight-turn input coil which is coupled to the washer shaped SQUID loop. In figure 3.3 the flux dependent voltage characteristic is given.
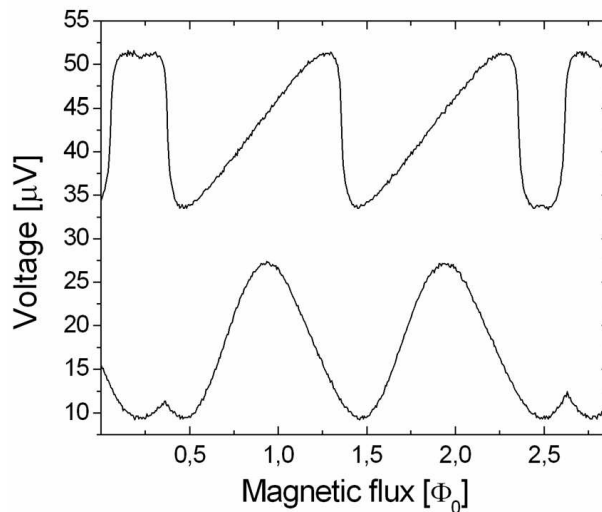
Figure 3.3 – Magnetic flux-voltage characteristic measured with [top] and without [bottom] APF

Its behavior, as in the typical magnetometer, shows that there are no resonances. The voltage swing and the responsivity of intrinsic characteristic are, respectively, 19.6μV and 62μV/Φ_0, such values are in good agreement with the predicted ones (18.0μV and 70μV/Φ_0). Note that the voltage swing of the characteristics with APF is a bit smaller than the intrinsic one; in fact, the APF resistor loads the SQUID, and so, it reduces the usable voltage swing.

Comparing the two responsivity, the APF increase the V_Φ of 12.9 times with respect to $V_{\Phi,intr}$, which corresponds to an APF gain of 0.92.

The flux-to-field conversion efficiency measured by applying an external magnetic field by means of calibrated Helmholtz coils is $B_\Phi = 3.2\,nT/\Phi_0$.

The magnetic flux to feedback current conversion factor (I_Φ) has been evaluated measuring the dc-current required to be sent in the feedback coil to obtain a sliding of one flux quantum in the V-Φ characteristics obtaining a

value as low as 7.4 µA/Φ_0. A low feedback current in FLL operations represent an important issue in large SQUID arrays to reduce cross-talk between the leading wires.
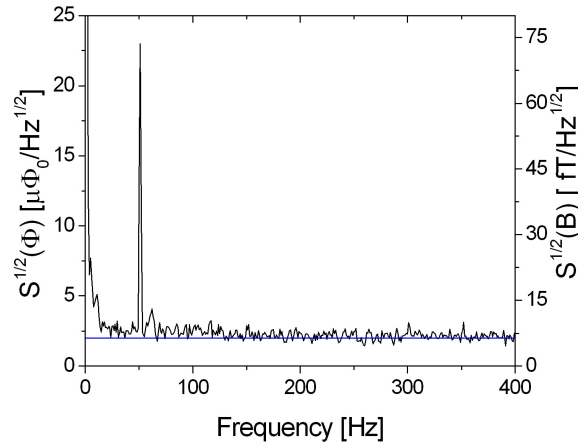

Figure 3.4 – Magnetic flux noise spectral density. The blue line indicates the theoretical estimated value. The corresponding magnetic field noise is also reported.

In Figure 3.4, the spectral density of both flux and magnetic field noise of the miniaturized SQUID magnetometer is reported. The sensor exhibits a magnetic flux noise level of 2.2 µΦ_0/√Hz in the white region corresponding to 7.0 fT/√Hz. The intrinsic SQUID noise obtained by subtracting the amplifier contribution is 5.8 fT/√Hz, which still remains the dominant term in the overall noise. Note that a more increase of APF gain, to furthermore decrease the amplifier noise, reduces both slew rate and bandwidth and could cause instability. However, to improve the readout performances, it is possible to use an ultra-low noise amplifier which is able to reach spectral density voltage noise as low as 0.3 nV/√Hz.

Again the 1/f corner is essentially due to the amplifier low frequency noise.

3.1.3   The planar gradiometer

The sensor consists of a fully integrated first order planar SQUID gradiometer having a baseline length d=50mm [9-11]. The pickup antenna consists of two rectangular coils having an area of 12×10 mm^2, arranged in a series configuration (cf. § 2.6.3).

Figure 3.5.a reports the flux to voltage characteristic showing a voltage swing as high as 65 µV while figure 3.5.b shows the responsivity as a function of the

applied magnetic flux obtained by taking the derivative of the V-Φ curve in a single period. A maximum V_Φ value of $500\mu V/\Phi_0$ has been found corresponding to about $0.3\Phi_0$ value.

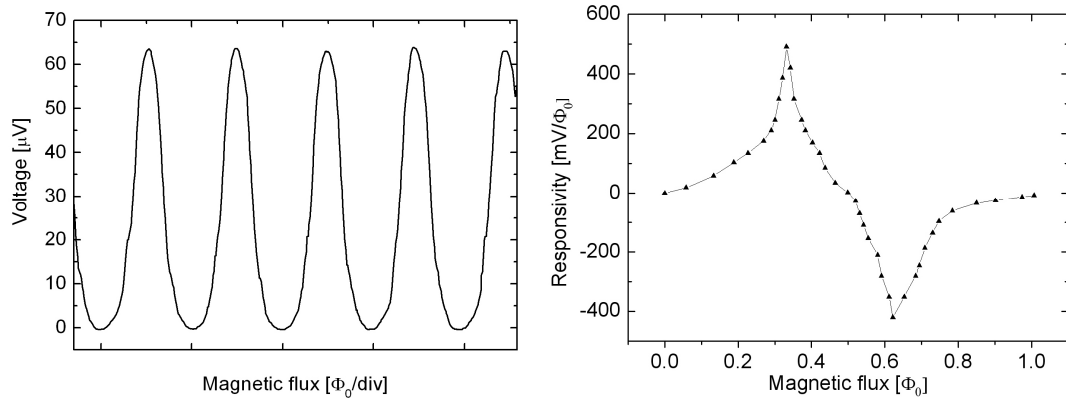

Figure 3.5 – a) Experimental voltage-magnetic flux characteristic and b) the magnetic flux dependent responsivity evaluated from the V-Φ

In Figure 3.6 the magnetic flux spectral density of a planar gradiometer [top] is reported and compared to a magnetometer having similar field sensitivity [bottom], both measured in flux looked loop. Since no high magnetic permeability shield is used, as expected the low frequency magnetic disturbances affect the magnetometer to a greater extent with respect to a gradiometer.
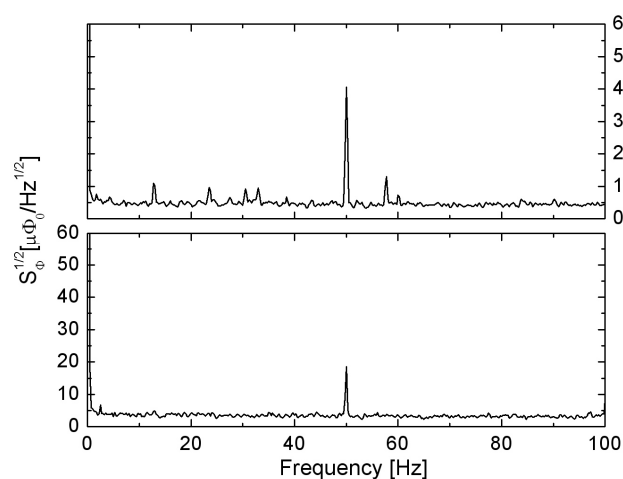

Figure 3.6 - Comparison of magnetic flux noise spectral densities of the planar gradiometer [bottom] and magnetometer having similar sensitivity [top]

3.1.4   The crosstalk measurements

The new generation of MEG system is based on a great number of sensors close-set, increasing the mutual disturbance. (cf. § 2.5)

In order to verify the effectiveness of the feedback coil design, the crosstalk measurement is carried out on the magnetometer reported above and compared to those performed on the similar sensor which differs only for having a typical square feedback coil [4-5].

To this aim, four SQUID devices have been arranged on a chip carrier, having the side dimension of 40mm, which may represent a cluster of possible sensor arrangement in a multichannel system; the distance between the sensor centers is 14mm (Figure 3.7) [5]. The area of square feedback coil is equal to 11mm^2 while the bipolar coil details are reported in the paragraph 2.5.1.
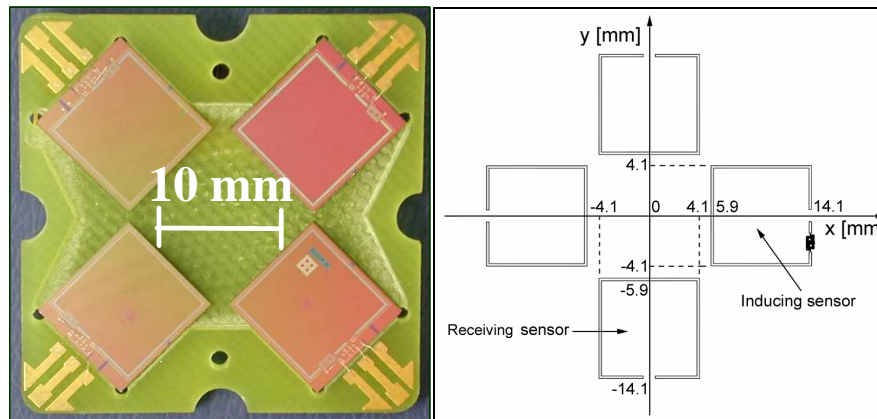

Figure 3.7 - Picture of a square board including four integrated dc-SQUID magnetometers having the new feedback coil design and, on the right, the drawing with the main distances.

Note that the magnetic field noise level, as reported in § 3.1.1, as low as 1.7 fT/Hz$^{1/2}$ ensure that the new feedback coil design, does not introduce any additional noise.

In the FLL operation mode, currents circulate in the feedback coils inducing a magnetic flux in the test sensor. The current value sent in the inducing feedback coils is what produces the saturation of the relative readout electronics, so as to maximize the signal to noise ratio. This value corresponds to a magnetic flux of about 100 Φ_0.

In figure 3.8 the output of receiving magnetometer when a sinusoidal current flows in the neighboring coils, is reported. The lower curve shows the output

signal relative to the bipolar feedback coil while the upper curve refers to square feedback coils. The crosstalk ranges from 2.8 % relative to square coil to 0.2 % for the bipolar feedback coil.
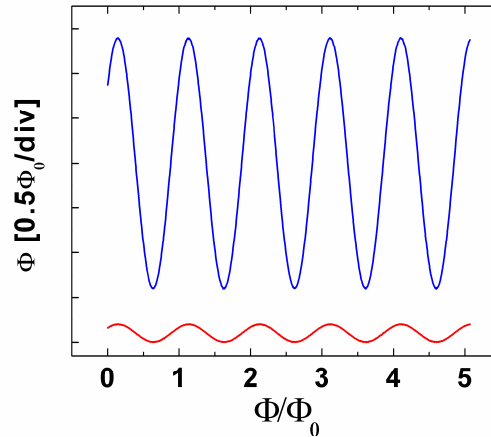

Figure 3.8 - SQUID magnetometer output in FLL mode produced by feedback coils of three inducing sensors arranged as in figure 3.7; the upper curve is relative to the square coil while the lower one refers to a bipolar coil (for the sake of clarity, the characteristics are vertically shifted).

Note that the crosstalk produced by the eight shaped coil is appreciably lower than the latter case. It is, also, due to a suitable design of the pickup coil which increases the inductive matching between feedback and pickup coils reducing the magnetic flux to feedback current transfer factor to $11\mu A/\Phi_0$ with respect to square coil value of $40 \ \mu A/\Phi_0$. The lower value of this transfer factor reduces the contribution due to the wire connections.

3.2   The MEG system

The MEG system shown in figure 3.9, consists of 163 fully integrated dc-SQUID magnetometers, having a pickup coil capture area of 64 mm^2, featuring adequate field sensitivity and bandwidth for brain imaging.
Among the different SQUID configuration investigated, the magnetometer one has been chosen since in the current configuration ensure the best field sensitivity [12]. Nevertheless, the system can be upgraded easily to use a larger   number of sensors; in this case the miniaturized magnetometer may be used provided that, to have the adequate sensitivity, the pickup coil side

length is at least 4 mm. Furthermore, the planar gradiometer may be used in biomagnetic system working in a soft shielding environment.

Since these sensors are placed close each to other, the integrated feedback coil for Flux-Locked-Loop (FLL) operation have been properly designed in a bipolar multiturn shape, in order to reduce the crosstalk effect between neighbor sensors.

Figure 3.9 – The 163 channels whole head MEG system

More than 200 SQUID magnetometer have been fabricated and characterized and selected on the basis of their performances. They are arranged on a multisensorial array designed and realized in a helmet shape. The measurement plane consists of 154 SQUID-channels suitably distributed over a fiberglass surface to cover the whole scalp and to record effectively the magnetoencephalographic signals.

Further 9 channels, installed on three bakelite towers (three triplet each having three orthogonal SQUID sensors), are used as references in order to detect background residual magnetic field far from the scalp (about 9 cm) and to subtract its contribution, via software properly implemented to this aim, from the brain signal detected on the measurement plane.

The sensor array, as shown by figure 3.10, is located in a fiberglass Dewar with a helmet shaped bottom, at a distance of 18 mm from the outside, where the head of patient is housed. The SQUID sensors are connected to the room temperature read-out electronics by means of more than 800 copper wires having a diameter of 0.08 mm and twisted in pairs to avoid a parasitic area. Furthermore, the helmet consists of three part conceived to allow both the insertion into the Dewar and the assembling on-site. To avoid any damage the helmet has been surrounded by thin fiberglass shields.

Figure 3.10 - The SQUID arrays in helmet shape containing 154 measurement channels and 9 reference sensors. On the right side: particular of a reference tower [top] and the helmet surrounded by the thin fiberglass shields [bottom]

The SQUID readout is a direct coupled electronics which can operate in flux locked loop mode and include additional positive feedback (see § 2.6.3), and is integrated in low-power, miniaturized boards; a single card drives six channels and is plugged in a shared motherboard located on the top of the dewar. In turn, the motherboard containing also the control logic unit and the filtering stage before the A/D conversion. The acquisition system may handles up to 600 channels, allows A/D conversion at frequencies up to 10 kHz. A remote console allows to manage the electronics parameters setting digital filtering, amplification, under-sampling, on-line average, and on-line software gradiometer composition based on selectable configuration files. Furthermore,

even if the SQUID tuning is automatically performed by the software, the operator can adjust manually the parameters to obtain the best performance. In figure 3.11, the helmet housed into the Dewar and the readout electronics at environmental temperature are shown.
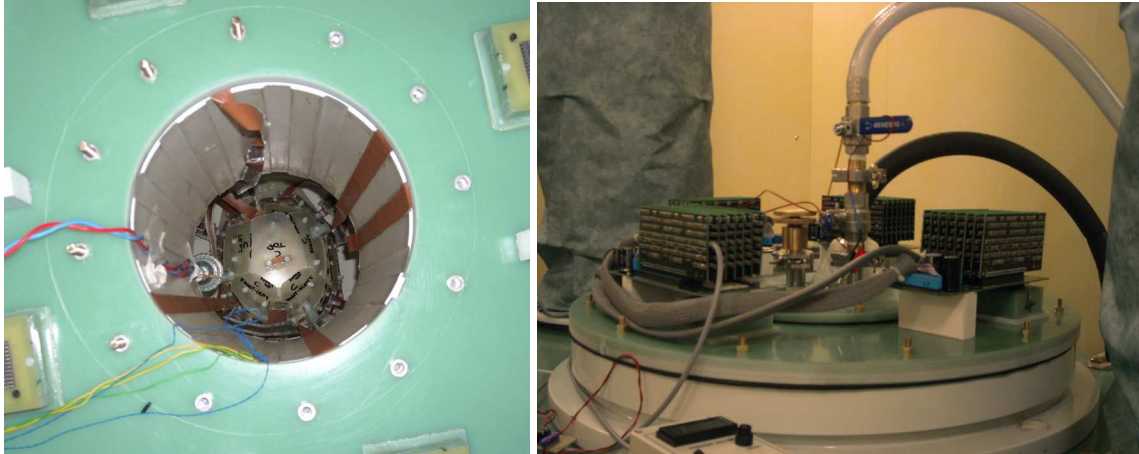

Figure 3.11 – The sensor array housed in the Dewar [left] and the SQUID electronics on the top of Dewar [right]

The system is equipped also with a 32 channels system for EEG allowing to record simultaneous both magnetic and electrical signals.

To eliminate any ambient disturbance the system operates in a suitable magnetic shielding room (MSR) designed on the basis of the environmental magnetic field measured on site before the installation.

Furthermore, a system for active compensation to further increase the MSR shielding factor have been designed and realized; this system generate a magnetic flux opposite to the environmental one by feeding in the helmholtz-like large coil a current automatically "locked" to incident field on the Magnetic shielding room, reducing the overall noise.

3.2.1   The Dewar design and performance

To keep the SQUID sensors below the critical temperature they are housed in a Dewar containing liquid helium at t=4.2K. It is made of non magnetic fiberglass having a *6mm* thick inner bottle and *8mm* thick the outside one. In order to reduce the distance of the sensor from the head, the thicknesses are reduced to *5mm* and *3 mm* respectively close to head housing. In such a way

the gap measures only 18mm. The capacity is 75 liters. In the figure 3.12, the drawing of the Dewar is shown together with the main dimensions.
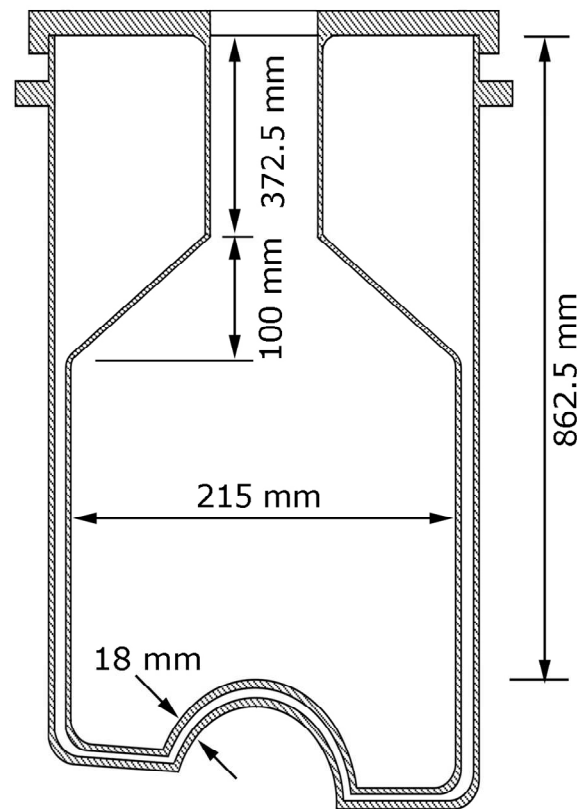

Figure 3.12 – Drawing of the fiberglass Dewar containing liquid helium (non scaled drawing size).

In the gap between the shells, a high vacuum is performed by a turbo molecular pump reaching, without liquid helium, a value as low as $2 \cdot 10^{-5}$ mbar; a further decrease of the inner pressure occurs when the Dewar is filled with liquid helium acting as cryogenic pump.

In order to verify the effectiveness of the Dewar a thermographic analysis has been performed. By using an infrared camera, the external temperature and its gradient have been evaluated. The results are reported in figure 3.13.

With an environmental temperature of 21°C, the minimum is reached in the left corner of the bottom Dewar where the temperature is 12.4 °C while in head housing the minimum temperature is 15.3 °C.
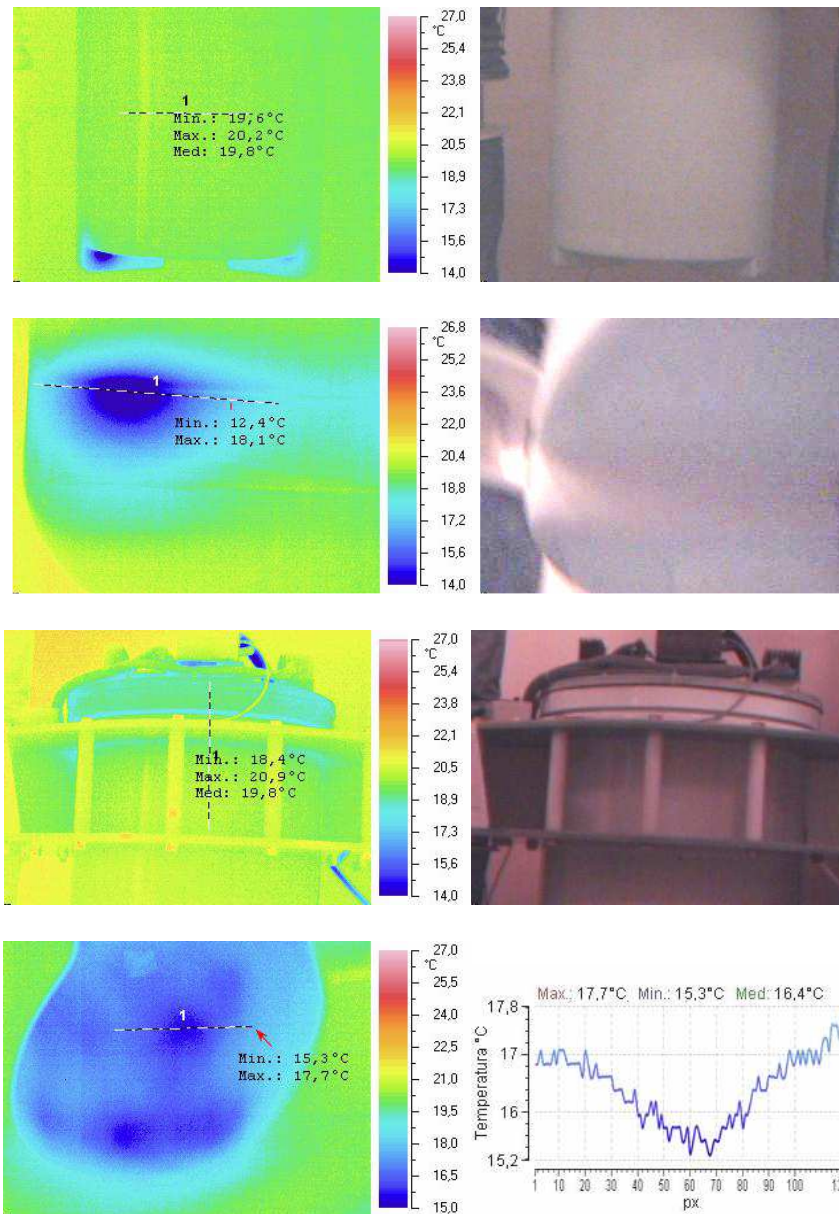
Figure 3.13 – Thermographic investigation of Dewar in its critical point. From the top: Bottom of Dewar; magnification of left corner; top of Dewar and finally, head housing.

As expected, the critical regions are located where the gap between the inner and outer shells is smaller. Nevertheless, these values are widely acceptable insomuch as the helium consumption of 100 liters/week is lower than the typical average.

The noise of the Dewar, about 1-2 fT/√Hz, is at most comparable than the noise of the SQUID sensors.

3.2.2   The magnetic shielding room performance

To avoid any environmental disturbance on the sensor measurement, the Dewar operate in Magnetically Shielded Room (MSR) (cf. §1.5.3), which consists of an external aluminum layer 12 mm thick and two inner layers of soft magnetic material having a thickness of 1.57 mm. Note that µ-metal (80% Ni, 14,5% Fe, 5% Mo, 0,5% Si, 0,02%Cu) has a magnetic permeability up to 45000 H/m. The gap between the µ-metal layers is 150mm in which an aluminum frame acts as a strucure.

Figure 3.14 – Particular of the shielding room (during the assembling) showing in clockwise direction: The µ-metal layer and the aluminum frame structure, the pneumatic door, the external aluminum door and outer aluminum layer.

The outer dimensions are: 3650mm×3300mm×3300mm.

The MSR is provided of an active compensation system as described in the paragraph 1.5.3. The Helmholtz like coils are wounded around the external perimeter of the MSR on each sides and have a maximum area of about $12m^2$. The shielding factor has been evaluated by feeding in the active compensation coil, (in open loop mode), a current generating a magnetic field of 10 µT and measuring the output signal of the selected SQUIDs sensor arranged along the directions x and y. The results are reported in figure 3.15.
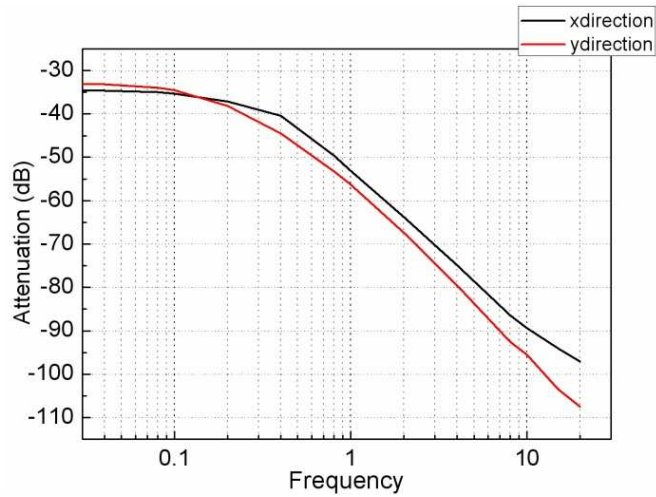
Figure 3.15 – Shielding factor of MSR

The resulting shielding factor is about 35 dB at 0.01 Hz, that increases up to 107 dB (y direction) and 97 dB (x direction) at 20 Hz. The slight difference at low frequency may be due to the presence of the door. The more consistent difference at relatively high frequency may be ascribable to different dimension of the MSR in x and y direction.

3.2.3   System characterization and first preliminary measurements

In figure 3.16 the SQUID magnetic field noise of SQUID group measured with MEG system is reported. The measurement was performed with no active compensation and no software gradiometer use.
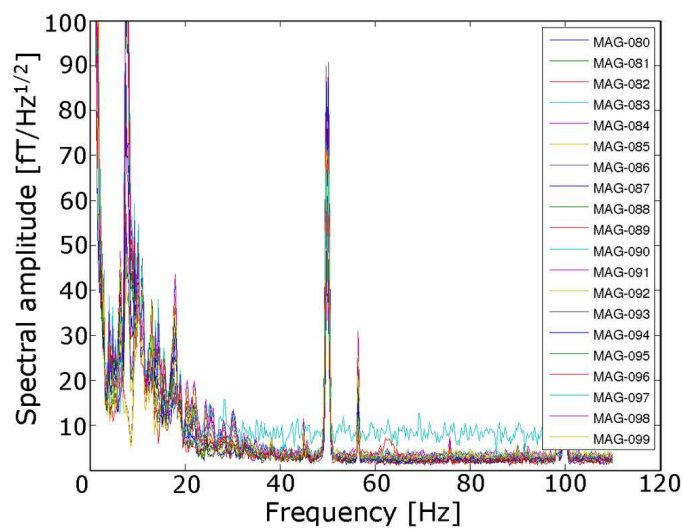

Figure 3.16 – Magnetic field noise spectral densities of a magnetometer cluster measured with empty MEG system

As evident there are a quite high noise in the frequency range 0÷20 Hz; above this range the mean noise level is less than 5 fT/√Hz

To investigate the noise source, the mechanical response of the MSR to external stress has been analyzed. To this aim, two seismographs have been placed inside and outside the MSR at a distance of 5 m each other, recording continuously the ground motion [13].

In figure 3.17, the velocity response spectrum evaluated for both outer and inner station respectively is reported; each trace corresponds to a 1-h-long time window. Note the significant difference day-night indicating that the noise is essentially due to human activities.
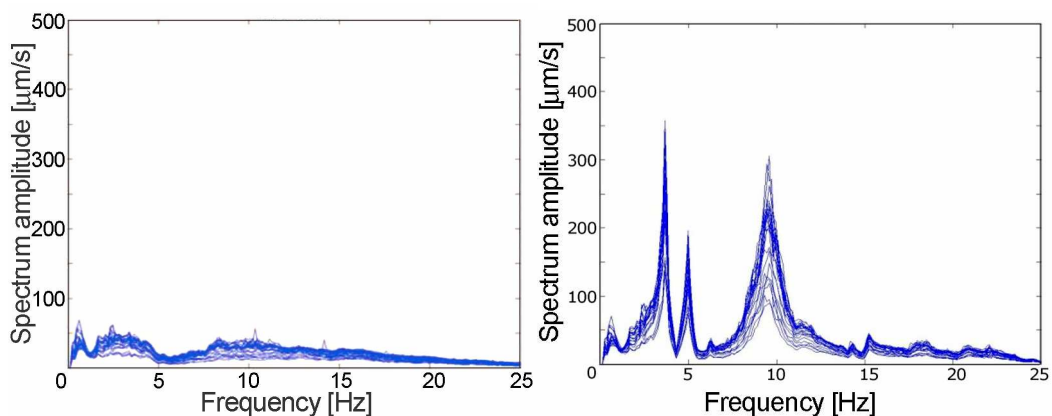

Figure 3.17 - Spectral amplitudes for the seismic signal recorded by the East-West components outside and inside the MSR respectively. Each line corresponds to a 1-h-long time window [13].

The noise level detected outside shows a constant level in the frequency range 1÷10 Hz having a few peak slightly higher than the ground level. The inside station shows the amplitude peaks at well localized frequency values with amplitude significantly higher than those the outside. Since for all traces, the ratio is held over the time, the response of the MSR can be considered elastic and assume that there is a resonance effect corresponding to external stress (both vertical and horizontal direction) in the range 1÷15 which are amplified up to a factor 10.

The noise level can be greatly decreased by using the software gradiometer. Since the background noise is effectively detected at the reference sensors level, this can be suitably detracted from the brain signal detected by the sensors located at measurement plane. The results is shown in figure 3.18
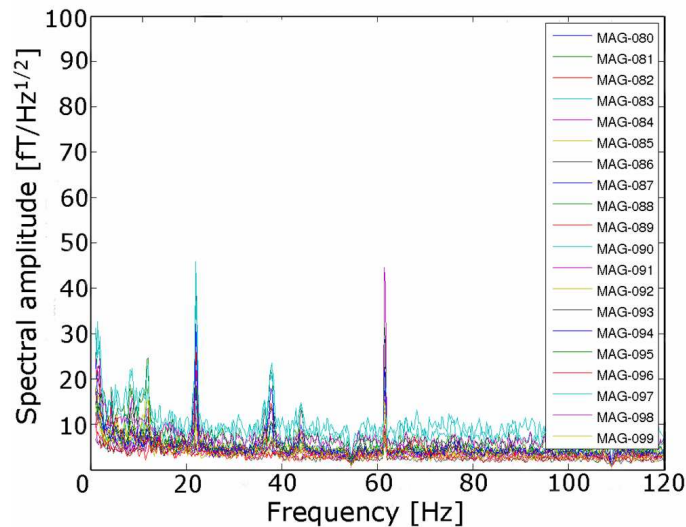
Figure 3.18 – Magnetic field noise spectral densities of the same previous magnetometer cluster obtained by using the software gradiometer method for noise cancellation

Note that the noise disturbances, at relatively low frequency, are clearly reduced. To test the effectiveness of this procedure a preliminary measurement has been performed to obtain the brain activity imaging corresponding to some tasks. The same recordings have been carried out, at same time, also with the embedded EEG system for comparison. The results are reported in figure 3.19.

The first measurement concerns a spontaneous activity: The so-called alpha rhythm, which appears in a human's brain awake but with eyes closed, has been recorded. The frequency range involved is 9-11 Hz.

The second one, concerns an evoked activity: the brain imaging during the forefinger tapping of a volunteer, has been recorded. The middle figure refers to the left finger tapping and, as expected, the activate motor cortex area is in the right hemisphere. In the bottom figure, instead, the imaging related to the movement of right forefinger is reported; as in the previous case, the contralateral area is involved. In this case the frequency signal are located around 7-9 Hz.

The good agreement between EEG and MEG imaging indicates that the system operates properly.

Closed eyes - Alpha Rhythm

Left forefinger - Motor Cortex Area
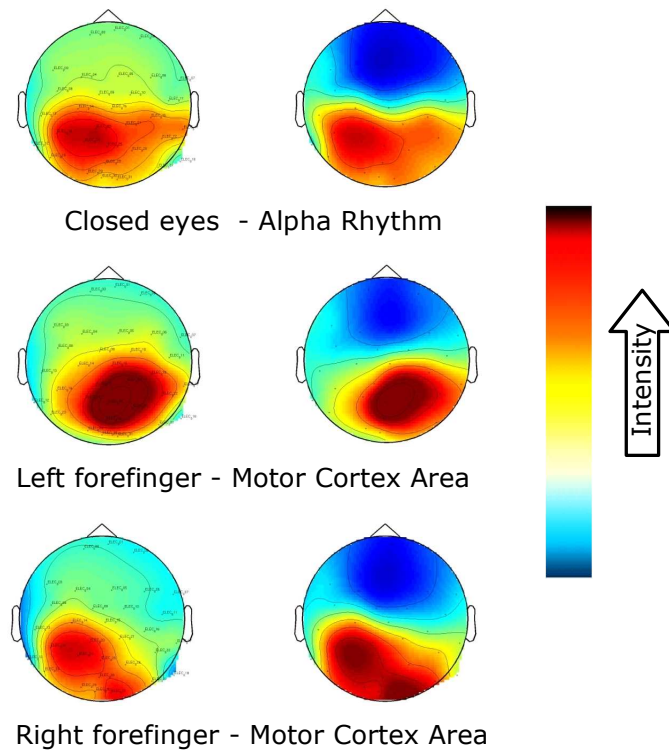
Right forefinger - Motor Cortex Area

Figure 3.19 – Preliminary measurement performed by the MEG system. The imaging refers to the activated brain areas detected by the MEG (right column) and EEG (left column) during a spontaneous activity (alpha rhythm) [top] and evoked activity (tapping of the left forefinger [middle] and the right forefinger [bottom])

Bibliography

1 C. Granata, A.Vettoliere and M. Russo IEEE Xplore DOI:10.1109/EURCON.2007.4400594, **556** (2007)

2 C.Granata, A.Monaco, C.Di Russo and M.Russo, Physica **C 368**, 227 (2002).

3 C.Granata, C.Di Russo, A. Monaco, and M. Russo, IEEE Trans. on Appl. Supercond. **11**, 95 (2001).

4 C. Granata, A. Vettoliere and M. Russo Appl. Phys. Lett. **88**, 212506 (2006);

5 A. Vettoliere, C. Granata, B. Ruggiero and M. Russo International Journal of Modern Physics **B 23**, 5759 (2009).

6 C. Granata, A. Vettoliere and M. Russo, Appl. Phys. Lett. **91**, 122509 (2007)

7 S. Rombetto, A. Vettoliere, C. Granata, M. Russo and C. Nappi, Physica **C 468**, 2328 (2008)

8 C. Granata, A. Vettoliere, S. Rombetto, C. Nappi, and M. Russo J. Appl. Phys. **104**, 073905 (2008)

9 C. Granata, A. Vettoliere, C. Nappi, M. Lisitskiy and M. Russo Appl. Phys. Lett. **95**, 042502 (2009)

10 A. Vettoliere, C. Granata, S. Rombetto and M. Russo, IEEE Trans. Appl. Supercond. **21**, 383 (2011)

11 A. Vettoliere, C. Granata, S. Rombetto and M. Russo, Sensors and Microsystems - AISEM 2010 Proceedings, Series: Lecture Notes in Electrical Engineering, Vol. 91 - ISBN 978-94-007-1323-9, Springer (2011)

12 S. Della Penna, C. Del Gratta, C. Granata, A. Pasquarelli, V. Pizzella, R. Rossi, M. Russo, K. Torquati and S. Ernè, Philosophical Magazine, **B80**, 937 (2000).

13 P. Cusano, A. Bobbio, G. Festa, S. Petrosino, S. Rombetto, Annals of Geophysics, **54**, 3 (2011).

Summary

A multichannel system for brain imaging containing 163 SQUID magnetometers arranged in a helmet shaped multisensorial array has been developed. To this aim, a previous investigation of a several SQUID configurations has been performed in order to choose a SQUID sensor having best performance for brain imaging on the basis of system working conditions. In particular, magnetometer and planar gradiometer have been designed, fabricated and characterized. Furthermore, a small magnetometer has been also taken into account. Since it has been decided to work in a magnetically shielding room a SQUID magnetometer has been chosen in order to guarantees high magnetic field sensitivity. These SQUID magnetometers are based on an integrated Ketchen design including a superconducting flux transformer consisting of a pickup coil and a multiturn input coil inductively coupled to the SQUID loop in a washer shape. The circuits for Flux Locked loop (FLL) operations and for Additional Positive Feedback including a thin film resistor network for gain adjusting, are integrated on the same chip containing the SQUID magnetometer. A magnetic field spectral noise as low as 1.8 fT/√Hz measured in FLL operation, ensures the sensor capability to detect the tiny magnetic filed arising from brain activity.

More than 200 SQUID magnetometers have been fabricated and characterized selecting the sensors with best performance.

154 measurement sensors are arranged in a SQUID multisensorial array properly designed and customized realized. Further 9 channels are located far from the scalp on three bakelite towers in order to realize via software a gradiometer to background noise rejection.

The system properties have been investigated including the estimation of background noise, the shielding factor of the magnetically shielding room and the Dewar performance.

Finally, preliminary measurements have been successfully performed. In particular, some brain activities such as the alpha rhythm, a spontaneous activity of a human having closed eyes and the evoked activity concerning the tapping of left and right forefinger have been analyzed.

The same activities have been co-registered using the 32-channels EEG to measure bioelectric activity. The good agreement between EEG and MEG data indicates that the system operates properly.